

Competing multiferroic phases in monolayer and few-layer NiI₂

Nanshu Liu^{1,2}, Cong Wang^{1,2}, Changlin Yan^{1,2}, Changsong Xu³, Jun Hu^{4*}, Yanning Zhang^{5*} and

Wei Ji^{1,2,5*}

¹*Beijing Key Laboratory of Optoelectronic Functional Materials & Micro-Nano Devices,
Department of Physics, Renmin University of China, Beijing 100872, China*

²*Key Laboratory of Quantum State Construction and Manipulation (Ministry of Education),
Renmin University of China, Beijing, 100872, China*

³*Key Laboratory of Computational Physical Sciences (Ministry of Education), Institute of
Computational Physical Sciences, State Key Laboratory of Surface Physics and Department of
Physics, Fudan University, Shanghai 200433, China*

⁴*School of Physical Science and Technology, Ningbo University, Ningbo, 315211, China*

⁵*Institute of Fundamental and Frontier Sciences, University of Electronic Science and Technology
of China, Chengdu, 610054, China*

**Corresponding authors. E-mail: hujun2@nbu.edu.cn; yanningz@uestc.edu.cn; wji@ruc.edu.cn.*

Abstract: A recent experiment reported type-II multiferroicity in monolayer (ML) NiI₂ based on a presumed spiral magnetic configuration (Spiral-B), which is, as we found here, under debate in the ML limit. Freestanding ML NiI₂ breaks its C_3 symmetry, as it prefers a striped antiferromagnetic order (AABB-AFM) along with an intralayer antiferroelectric (AFE) order. However, substrate confinement may preserve the C_3 symmetry and/or apply tensile strain to the ML. This leads to another spiral magnetic order (Spiral-IV^X), while 2L shows a different order (Spiral-V^X) and Spiral-B dominates in thicker layers. Thus, three multiferroic phases, namely, Spiral-B+FE, Spiral-IV^X+FE, Spiral-V^X+FE, and an anti-multiferroic AABB-AFM+AFE one, show layer-thickness-dependent and geometry-dependent dominance, ascribed to competitions among thickness-dependent Kitaev, biquadratic, and Heisenberg spin-exchange interactions and single-ion magnetic anisotropy. Our theoretical results clarify the debate on the multiferroicity of ML NiI₂ and shed light on the role of layer-stacking-induced changes in noncollinear spin-exchange interactions and magnetic anisotropy in thickness-dependent magnetism.

Keywords: NiI₂, multiferroics, spiral magnetism, monolayer, layer dependence

Magnetoelectric (ME) effects enable the manipulation of magnetic (electric) properties using electric (magnetic) fields, which is of interest in terms of both fundamental physics and potential spintronic applications [1, 2]. ME manipulations can be achieved by multiferroic materials exhibiting magnetic and electric orders [3]. Usually, the electric polarization of a type-II multiferroic material is induced by a magnetic order spontaneously through the inverse Dzyaloshinskii–Moriya (D–M) interaction [4-7]. However, the fact that the identification of type-II multiferroics in atomically thin van der Waals (vdW) monolayers (MLs) is still under debate. NiI₂ is a highly promising candidate for ML multiferroicity. Its bulk form undergoes two successive magnetic phase transitions [8, 9] from a paramagnetic (PM) phase to an interlayer antiferromagnetic (AFM) phase at $T_{N1} = 76$ K and then to a spiral magnetic phase below $T_{N2} = 59.5$ K [8]. The AFM-to-spiral transition is accompanied by breaks of both rotational and inversion symmetries, which results in electric polarization through the inverse D–M interaction. This effect is reflected in second harmonic generation (SHG) [10] and birefringence signals [11].

Monolayer NiI₂ on an hBN substrate was recently shown to exhibit multiferroicity under 20 K as its enhanced SHG signal strength [11], ascribed to a broken inversion symmetry of either magnetic or geometric (electrical) origin. However, the magnetic configuration of ML NiI₂ below 20 K remains an open issue, as no direct experimental measurement has been successfully conducted and previous density functional theory (DFT) predictions are under debate among ferromagnetic (FM) [12-14], helimagnetic [15, 16], and AFM [17] configurations. Although not conclusive, they are indeed different from the bulk groundstate. If the SHG enhancement originates from the magnetic contribution, it cannot guarantee the formation of additional electric polarization below 20 K [11]. This concern about the claimed multiferroicity was reinforced by the fact that no SHG enhancement was observable in ML NiI₂ on a SiO₂ substrate [10]. Therefore, the assertion of multiferroic ML NiI₂ requires further verification beyond the SHG measurement [11], which raises the question of whether type-II multiferroicity persists in the ML limit.

In this work, we examine the evolution of the magnetic groundstate and electric polarization of NiI₂ from the bulk to the ML using DFT calculations. We suggest a tentative layer-dependent magnetic phase diagram that illustrates the competition among, at least, four magnetic phases, with three spiral ones (one collinear) being (anti-)ferroelectric and induced by the inverse D–M interaction. The magnetic groundstate of ML highly depends on the in-plane geometry to stabilize the competing Spiral-IV^X (q_{IV}^X) and AABB-AFM configurations under different strains. We additionally demonstrate that these phase changes are driven by the competition among layer-thickness and local-geometry-dependent (non-)collinear Kitaev, biquadratic, and isotropic Heisenberg spin–exchange interactions and single-ion anisotropy. We also construct NiI₂/hBN and NiI₂/SiO₂ heterostructures to consistently explain the SHG signal of ML NiI₂ over 20 K obtained by two pioneering experiments [10, 11].

The spin–exchange coupling parameters were extracted based on the following Hamiltonian[18]

$$H = -\frac{1}{2} \left[\sum_{i,j;x,y,z} J_{ij} \mathbf{S}_i \cdot \mathbf{S}_j + \sum_{i,j;x,y,z} J_{ij}^{\perp} \mathbf{S}_i \cdot \mathbf{S}_j + \sum_{i,j;\alpha,\beta(\gamma)} \left(\lambda_{\alpha} S_i^{\alpha} S_j^{\alpha} + \lambda_{\beta} S_i^{\beta} S_j^{\beta} + \lambda_{\gamma} S_i^{\gamma} S_j^{\gamma} \right) + \sum_{i,j} B (\mathbf{S}_i \cdot \mathbf{S}_j)^2 + 2 \sum_{i;x,y,z} A_z S_i^z \right] = -\frac{1}{2} \left[\sum_{i,j} J_{ij} \mathbf{S}_i \cdot \mathbf{S}_j + \sum_{i,j} J_{ij}^{\perp} \mathbf{S}_i \cdot \mathbf{S}_j + \sum_{i,j} (K_{ij}^{\gamma} S_i^{\gamma} S_j^{\gamma}) + \sum_{i,j} B (\mathbf{S}_i \cdot \mathbf{S}_j)^2 + 2 \sum_i A_z S_z^2 \right],$$

where A_z represents the single-ion anisotropy, J_{ij} and J_{ij}^{\perp} are the intra- and inter-layer isotropic Heisenberg exchange parameters, B and K_{ij}^{γ} are the biquadratic and collinear Kitaev interaction parameters [19]. We followed the procedures used in our previous calculations [20, 21] and have included the details in the [Appendix-A](#).

Bulk NiI₂ crystal has a rhombohedral structure in space group $R\bar{3}m$ at room temperature ([Fig. 1a](#)), comprised of triangularly arranged Ni²⁺ cations ($3d^8$, $S=1$) and coordinating I anions. We used a $1 \times \sqrt{3} \times 1$ supercell to more clearly show magnetic configurations in [Fig. 1e](#). The calculated lattice constants $a = 3.926 \text{ \AA}$, $b = 6.790 \text{ \AA}$,

and $c = 19.744 \text{ \AA}$ of bulk NiI_2 crystal in the experimentally observed spiral order (Spiral-B), consistent with the experimental values of $a = 3.919 \text{ \AA}$, $b = 6.765 \text{ \AA}$, and $c = 19.635 \text{ \AA}$ [22]. Spiral-B exhibits a propagation vector $q_B = (0, 0.138, 1.457)$ (Figs. 1c and 1d) below $T_{N2} = 59.5 \text{ K}$ [11, 22]. Note that in the coordinates defined in the literature [11, 22], $q_B = (0.138, 0, 1.457)$. Our DFT calculations reproduced this magnetic order suggested in experiments [11, 23] and obtained by a spin Hamiltonian [24] in which Spiral-B exhibits the lowest energy compared to the five collinear magnetic configurations (Fig. 6 in Appendix-B) and 55 other spiral configurations with different q values (Figs. 1e and 1f). The Spiral-B groundstate is robust regardless of the preservation of the C_3 symmetry (Table I), consideration of spin-orbit coupling (SOC) (Fig. 7), and choice of on-site Coulomb interaction (U_{eff}) values (Fig. 8). We are thus confident of the reliability of our results for ML or few-layer NiI_2 .

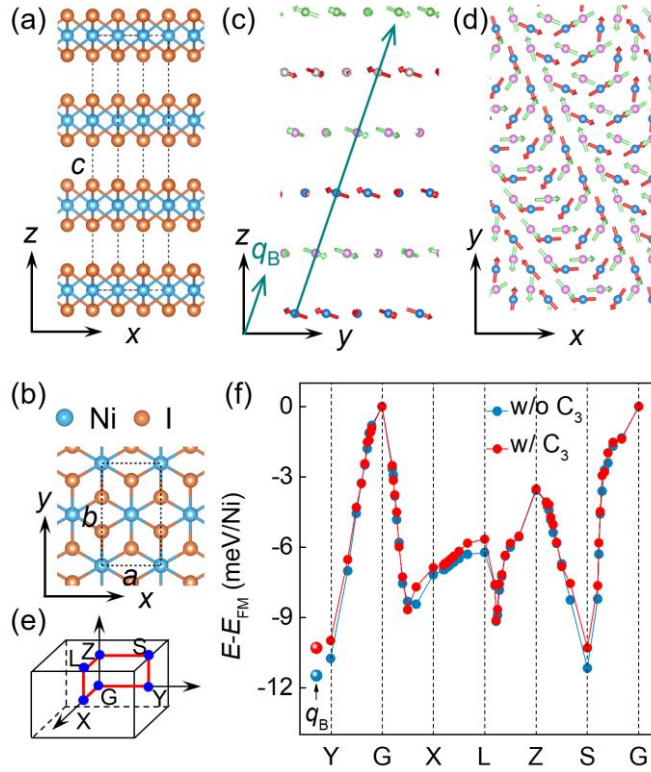


FIG. 1. Side (a) and top (b) views of the atomic structure of bulk NiI_2 . Schematics of Spiral-B in side (c) and top (d) views. Only two Ni layers were plotted in (d) to more clearly show the magnetic moments. (e) q -path considered in the first Brillouin zone of a $1 \times \sqrt{3} \times 1$ supercell. (f) Relative energies of all considered spiral orders with (red) and without (blue) preserved C_3 structural symmetry.

The magnetism of ML and few-layer NiI_2 is more complicated than bulk NiI_2

and difficult to be captured by a spin Hamiltonian. We considered 25 collinear and 71 non-collinear magnetic orders using the supercell model and a 10×10 q -mesh for the generalized Bloch theorem (gBT) model to explore the layer-dependent magnetic groundstates. We focus on the geometries showing (ML-C3) and not showing (ML-NC3) the C_3 symmetry for the ML because the geometric symmetry is more easily modulated by the substrate [25-27]. For thicker layers, up to 4L, we concentrate on constraint-free geometries as the substrate constraint rapidly relaxes in thicker layers [28].

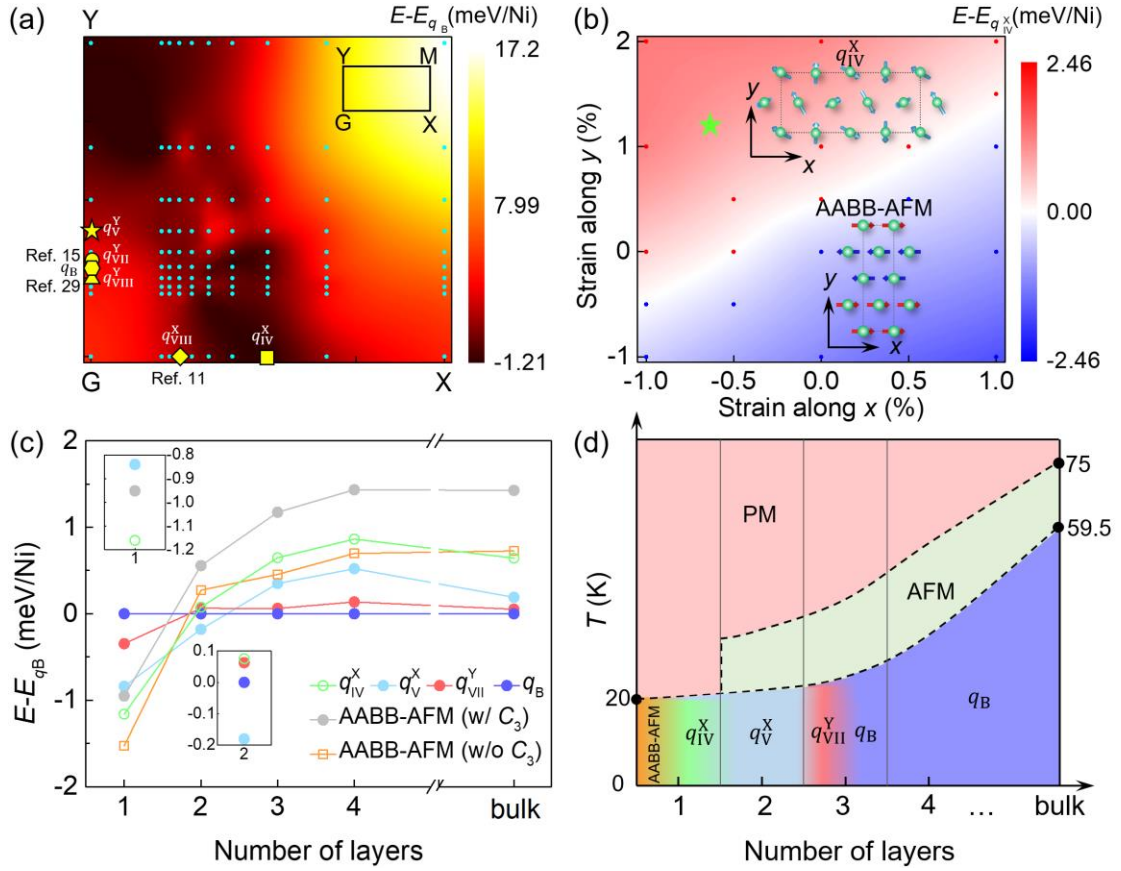


FIG. 2. (a) Energy difference mapping between spin-spiral and Spiral-B orders for ML-C3. Inset: q -path in the first Brillouin zone of a $1 \times \sqrt{3}$ supercell. The spiral vectors in bulk NiI_2 (q_B), Spiral-IV^X (q_{IV}^X), Spiral-V^Y (q_V^Y), Spiral-VIII^X (q_{VIII}^X) from Ref. [11], Spiral-VII^Y (q_{VII}^Y) from Ref. [15] and Spiral-VIII^Y (q_{VIII}^Y) from Ref. [29] are indicated by yellow polygons. (b) Energy difference between AABB-AFM and Spiral-IV^X versus epitaxial strains along the x and y directions for ML-NC3. Inset: top views of Spiral-IV^X and AABB-AFM orders. The green star denotes the strain values of ML NiI_2 being applied from an $h\text{BN}$ substrate. The original data was represented by colored dots in (a) and (b). (c) Layer-dependent energy difference between the spin-spiral and Spiral-B orders for both structures. Inset: zoomed-in energies for ML and 2L NiI_2 . (d) Schematic magnetic phase diagrams for different NiI_2 layers

versus temperature, with PM and AFM representing paramagnetic and interlayer AFM states, respectively. The transition temperatures were taken from an experimental work [30].

Figure 2a (Figure 9 in Appendix-C) plots an energy map (profile) for the q -mesh (differently sized supercells) of ML-C3 NiI₂, where the C_3 symmetry is preserved under constraint. In the following, all energy comparisons were based on the results by constructing supercells including SOC. Both plots indicate a new spiral configuration (Spiral-IV^X, upper inset in Fig. 2b), the magnetic moments of which align in the Ni-I plane and follow the propagating vector $q_{IV}^X = (0.250, 0, 0)$ (across each $4 \times \sqrt{3}$ supercell, Figs. 10a and 10b), consistent with a recently spin-polarized scanning tunneling microscopy (SP-STM) observation [31], and same as a previous work but with magnetic moments rotating in the yz plane [32]. Spiral-IV^X shares the same propagation direction with the spiral order discussed in Ref. [11] (Spiral-VIII^X) where the propagating period twice that of Spiral-IV^X, namely eight-unit cells (Fig. 11). Spiral-IV^X is, at least, 0.16 meV/Ni more stable than the other spiral orders listed in Table II (e.g., Spiral-V^Y, Spiral-VII^Y, and Spiral-B; see Fig. 2c) and a collinear AABB-AFM order (lower inset in Fig. 2b), while other configurations (Figs. 12 and 13) are even less stable than the abovementioned five. Spiral-IV^X is also more stable by at least 0.81 to 1.75 meV/Ni than the two recently theoretically suggested [15, 29] and one experimentally observed [33] spiral orders.

In the constrain-free case, the AABB-AFM structure breaks the C_3 symmetry (ML-NC3), which is more stable than Spiral-IV^X by 0.35 meV/Ni (Table II and Fig. 2c). This suggests that external strain plays a role in tuning their relative stability. As shown in a phase diagram in Fig. 2b, Spiral-IV^X is substantially stabilized under in-plane compressive strain along the x direction and/or tensile strain along the y direction (red zone in Fig. 2b). Order Spiral-IV^X is, at least, 0.12 meV/Ni more stable than Spiral-V^Y and Spiral-VII^Y in the whole considered strain range, while order AABB-AFM becomes even more stable than order Spiral-IV^X in certain strain regions (Fig. 14 in Appendix-D). Thus, the magnetic groundstate was compared between Spiral-IV^X and AABB-AFM orders for simplicity.

For constrain-free 2L NiI₂, the AABB-AFM order becomes less stable compared to those spiral orders. A new spiral order, Spiral-V^X (q_V^X), emerges and is 0.26 meV/Ni more stable than Spiral-IV^X. Spiral-V^X also propagates in the x direction, following vector $q_V^X = (0.20, 0, 0)$, almost degenerated with the order observed in the SP-STM experiment [31], where a spiral order exhibits $5.01a$, deviating by 7° from the x direction. Spiral-V^X is more stable than Spiral-VII^Y (q_{VII}^Y) and Spiral-B by 0.24 and 0.18 meV/Ni, respectively (Table III in Appendix-E, Fig. 2c), nearly energetically undistinguishable. Here, Spiral-VII^Y propagates along the y direction across a 1×7 supercell and represents the in-plane projection of Spiral-B, indicating that the interlayer non-collinear spin–spin interactions are rather weak compared to their in-plane counterparts. Breakdown or preservation of the C_3 symmetry does not essentially change the relative stability of these spiral orders (Table III).

Spiral-VII^Y and Spiral-B are still energetically undistinguishable in 3L, but over 0.35 meV/Ni more stable than Spiral-IV^X and Spiral-V^X (Table IV). In 4L and thicker layers, the interlayer spin–spin interactions play a more crucial role as Spiral-B becomes the groundstate by at least 0.14 meV/Ni (Table V). These results depict a layer-dependent competition of one collinear and four spiral orders within four layers, as schematically summarized in the magnetic phase diagram (Fig. 2d).

We examined the impact of U_{eff} and functional on relative energies of those competing configurations. The U_{eff} values up to 5.4 eV don't affect their relative stability (Fig. 15a in Appendix-F) and are already larger than the values used in the literature [34] and obtained by a linear response method [35]. Their stability was also verified using the Perdew–Burke–Ernzerhof (PBE), PBE-D3, Revised PBE, and HSE06 hybrid functionals considering SOC (Fig. 15b), despite numerical discrepancies between the results obtained from HSE06 and other functionals.

Orders Spiral-IV^X, Spiral-V^X, and Spiral-B (Spiral-VII^Y) induce electric polarization through the inverse D–M interaction, represented by $\mathbf{P} \parallel \hat{\mathbf{e}} \times \mathbf{q}$, where $\hat{\mathbf{e}}$ denotes the rotational axis of the spiral spins [36]. In Fig. 3a, the clockwise-rotating spins propagating along the x direction in the q_{IV}^X generate an in-plane electric

polarization in the y direction (P_y), perpendicular to bulk in the experiment [8]. A switchable polarization vector characterizes an FE material rather than an electret. Figure 3b illustrates a likely intermediate configuration in a switching process of rotating spins propagating from the $+x$ (q_{IV}^X) to the $-x$ direction ($-q_{IV}^X$, Fig. 3c). The change in the propagating direction switches the electric polarization from the $+y$ (Fig. 3a) to the $-y$ (Fig. 3c), surmounting an energy barrier of ~ 6 meV in ML-C3 NiI₂ (Fig. 16a in Appendix-G), which is comparable to that of FE ML SnSe (3.76 meV) [37] but smaller than FE ML Bi (43 meV) [38]. The electric polarizations for Spiral-VII^Y and Spiral-B are in the x direction (P_x) for their propagating directions along the y direction. In Fig. 3d, the bulk value of 0.90 pC/m (for Spiral-B) gradually drops to 0.24 pC/m in ML-C3 (Spiral-IV^X), comparable to the values for ML FeOCl (~ 0.39 pC/m) [39] and ML Hf₂VC₂F₂ (0.29 pC/m) [40].

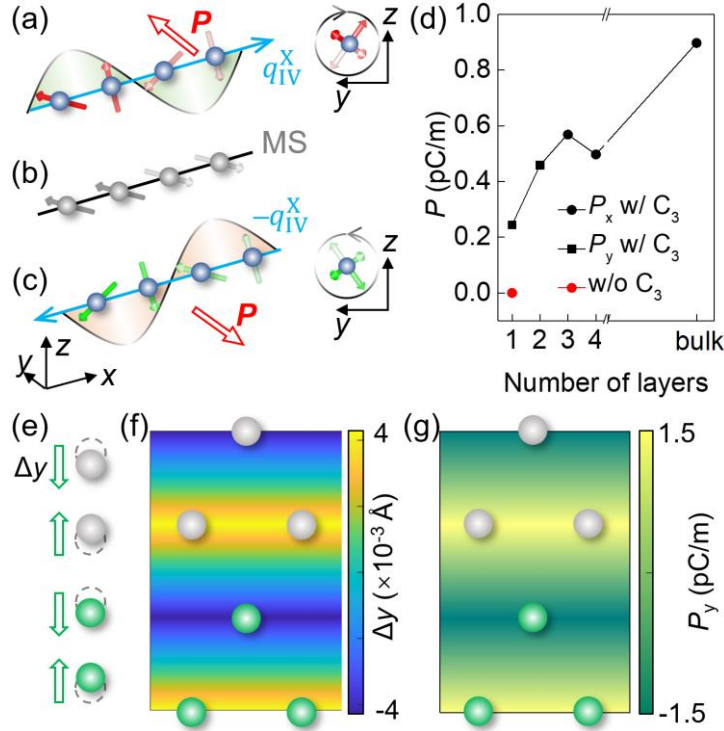


FIG. 3. Schematic plots for a spin canting process from (a) a clockwise propagation in Spiral-IV^X (q_{IV}^X) to (c) a counterclockwise one ($-q_{IV}^X$) through (b) a likely metastable state (MS). The (counter-)clockwise spin spiral generates an in-plane electric polarization (anti-)parallel to the y direction. (d) Theoretical electric polarization versus the number of NiI₂ layers. (e–f) Displacement of Ni atoms in AABF-AFM along the y direction in ML-NC3. (g) Electric polarization induced by displacements of Ni atoms in the AABF-AFM state.

However, the AABB-AFM order in ML-NC3 eliminates the total electric polarization and exhibits intralayer antiferroelectricity for the shrank lattice along the y -axis accompanying with Ni atoms relaxation (Table VI and Fig. 3e). The Ni atoms in the same AFM stripe move oppositely by 0.004 \AA in the $\pm y$ directions (Fig. 3f), yielding a dipole moment of $\pm 1.5 \text{ pC/m}$ (Fig. 3g). The switching barrier (Fig. 16b) between the two AFE configurations is $\sim 6 \text{ meV}$, comparable to the FE barrier of ML Spiral-IV^X.

In short, few-layer NiI₂ exhibits at least four competing multiferroic phases: the newly found Spiral-IV^X + FE, Spiral-V^X + FE, and AABB-AFM + AFE states and the previously known Spiral-B + FE state. Thus, ML NiI₂ is indeed a type-II multiferroic material, but with tunable multiferroicity between AFM + AFE and Spiral + FE by the in-plane geometry. This helps explain the seemingly contradictory experimental results [10, 11], where ML NiI₂ was supported on SiO₂ [10] and *h*BN [11] substrates, suggesting the substrate may play a role in affecting their in-plane geometry.

The ML NiI₂ was epitaxially grown on a *h*-BN substrate [11], while the structural details of ML-NiI₂ on the *h*-BN substrate remain unknown in experiments. We thus theoretically considered the ML-NiI₂/*h*-BN interface exhibiting the smallest lattice mismatch and lowest total energy [41]. We used an ML NiI₂ $10 \times 4\sqrt{3}$ / ML *h*BN $9\sqrt{3} \times 11$ -R30 rectangular supercell, in which the *h*BN substrate applies a compressive strain of -0.6% along the x direction and a tensile strain of $\sim 1.3 \%$ along the y to ML NiI₂. This supercell is 1.43 and 2.48 meV/Ni more stable than the two configurations (Fig. 17 in Appendix-H) exhibiting the second and third smallest interfacial strains, which are in the tensile strain region. The Ni layer (Fig. 18a) and the two I sublayers (Fig. 19) exhibit out-of-plane corrugations varying up to 0.06 \AA . Nonuniform in-plane strains further break the inversion symmetry in the x (Fig. 18c) and y (Fig. 18d) directions. Moreover, explicit interfacial charge transfer from the BN layer to the interfacial I layer leads to an out-of-plane electric polarization (Figs. 18e and 18f). Therefore, ML NiI₂ on *h*BN simultaneously breaks its structural inversion symmetry, corresponding to the observable SHG signals above 20 K in Ref. [11].

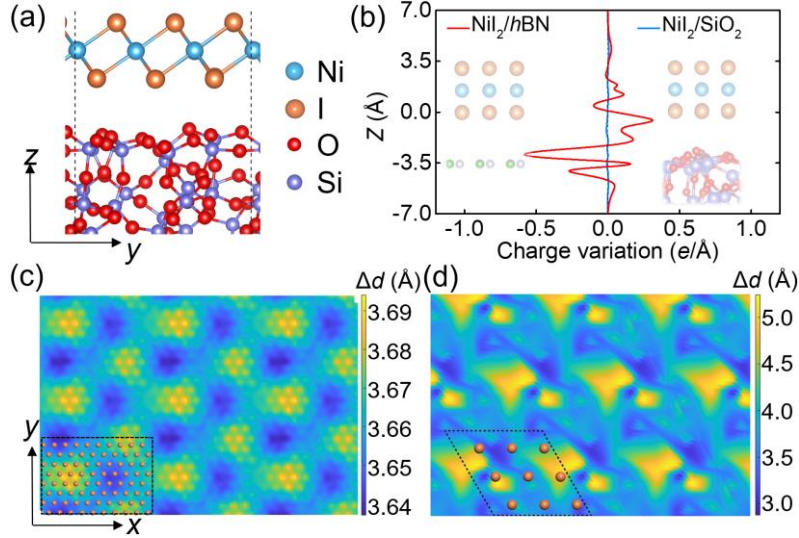


FIG. 4. (a) Side view of the optimized geometrical structure of a NiI₂ ML deposited on an amorphous SiO₂ substrate. (b) Line profiles along the z direction of charge variations for the NiI₂/h-BN and NiI₂/SiO₂ heterostructures. The z -coordinates of the interfacial I atoms were set to zero. 2D mappings of spatial variation of vertical distances between lower I atoms and (c) top-layer B or N atoms of the h -BN substrate and (d) surface O atoms of the SiO₂ substrate.

These strong modifications from the h BN to ML NiI₂ indicate their strong interactions. NiI₂ is, most likely, prone to maintain its C_3 symmetry on h BN due to the confinement from the C_3 symmetrized h BN. For ML-C3, Spiral-IV^X is preferred over AABB-AFM and further stabilized under biaxial compressive strains and electron doping (Figs. 14b and 20 in Appendix-I). Thus, the SHG signal could be further enhanced by the additional in-plane electric polarization induced by the noncollinear Spiral-IV^X order formed below 20 K [11]. However, the amorphous SiO₂ substrate is a well-saturated substrate that exhibits weak interactions with its supporting MLs [42]. The validity of this statement for ML NiI₂ was supported by our theoretical comparison of the NiI₂/SiO₂ and NiI₂/hBN interfaces (Fig. 4 and Appendix-J), in which the NiI₂/SiO₂ interface shows negligible interfacial charge variations (Fig. 4b) and larger interfacial distance variations (Figs. 4c and 4d). The SiO₂ substrate thus interacts more weakly to NiI₂, leading the NiI₂ overlayer more close to its freestanding form. Therefore, ML NiI₂ placed on amorphous SiO₂, most likely, favors the collinear AABB-AFM order and thus shows no temperature-dependent SHG enhancement [10].

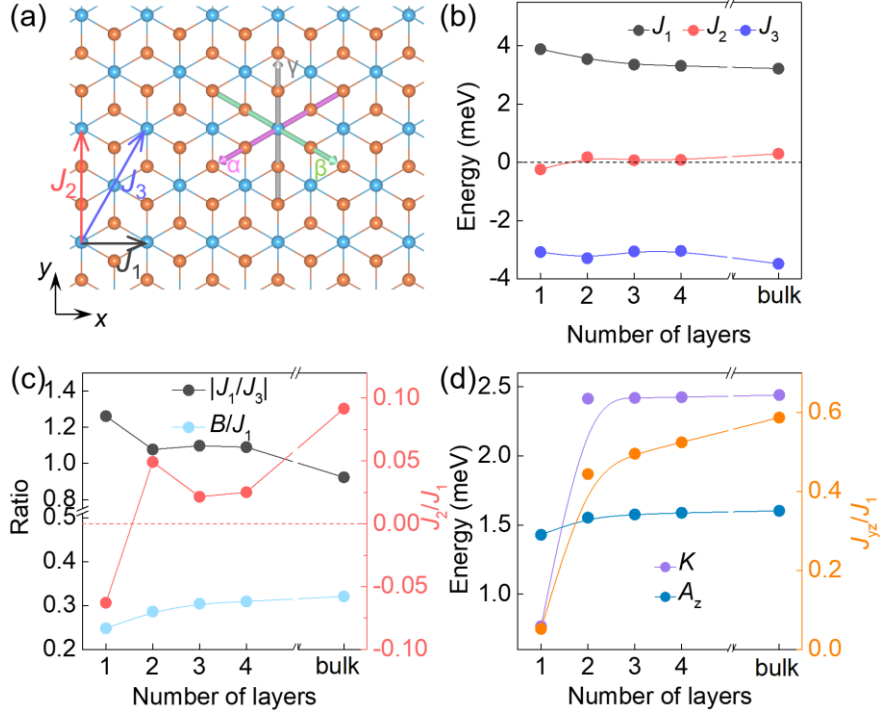


FIG. 5. (a) Schematic illustration of the Kitaev basis $\{\alpha\beta\gamma\}$ (magenta, green, and grey arrows) and the intralayer isotropic first to third nearest-neighbor Heisenberg spin-exchange parameters J_1 to J_3 . (b) Layer-dependent evolution of J_1 , J_2 , and J_3 . (c) Ratios of $|J_1/J_3|$, J_2/J_1 , and B/J_1 . (d) Non-collinear J_{yz} over J_1 (J_{yz}/J_1), Kitaev K and single-ion anisotropy A_z .

The remaining issue is why ML and few-layer NiI_2 hosting at least four competing states. We plotted the layer dependence of various magnetic interactions (Fig. 5). Parallel coupled Heisenberg J_1 (black in Fig. 5a) nearly maintains its bulk value of 3.22 meV down to 3L and then rapidly increases to 3.55 meV in 2L and 3.89 meV in ML (Fig. 5b). Anti-parallel coupled J_3 (blue in Fig. 5a) exhibits almost the opposite trend (Fig. 5b). Their competition could lead to non-collinear spin spiral states if $|J_1/J_3| < 4$ [43]. The DFT revealed that $|J_1/J_3|$ ranges from 0.92~1.26 for NiI_2 layers (Fig. 5c) and fits this criterion well, while the strongest (weakest) frustration occurs in bulk (ML) where the ratio reaches its minimum (maximum) among all considered layer thicknesses.

Two-site anisotropy J_{yz} characterizes the preference of the direction of magnetic moments canting from the xy -plane to the z -axis [29]. The bulk NiI_2 exhibits $J_{yz} = 1.90$ meV and the largest J_{yz}/J_1 ratio of 0.59 (Fig. 5d), indicating the preferred out-of-plane (OOP) orientations of the magnetic moments in thicker layers, consistent to

their OOP easy axes (Figs. 21b and 21c in Appendix-K) and in-plane one in ML (Fig. 21e). Single-ion anisotropy A_z , favoring the moments oriented in the z -axis, follows the same trend and reaches its maximum positive value of 1.60 meV (Fig. 5d) in bulk NiI_2 . A considerably large Kitaev interaction $K = 2.44$ meV (see Fig. 5d) confines magnetic moments in the α - β plane (Fig. 1c), which leads to Spiral-B being more stable than its xy -plane projection Spiral-VII^Y. The moments in Spiral-B are slightly off the α - β plane owing to competition between K and A_z .

For layers thinning from bulk down to 4L-2L, the ratio between the competing FM J_2 and J_1 (J_2/J_1) decreases from approximately 0.03 (4L) to 0.02 (3L) and then increases to 0.05 (2L) (Fig. 5c), which results in the emergence of a spatially smaller spiral order (Spiral-V^X) in 2L. However, configurations Spiral-B and Spiral-VII^Y are energetically indistinguishable in 2L, because of multiple competing interactions such as the slightly reduced A_z , and nearly unchanged $|J_1/J_3|$ ratio and K . The second interlayer nearest neighbor exchange parameter (J_2^\perp) is AFM and dominates for bulk to 2L (Tables VII and VIII in Appendix-L), resulting in interlayer AFM couplings between NiI_2 layers.

In the ML limit, the ratio J_2/J_1 changes to be negative with a larger value of -0.06 (Fig. 5c), which, together with parallel coupled biquadratic magnetic dipole interaction B , leads to the competed AABB-AFM and Spiral-IV^X configurations. The ratios of B and J_2 over J_1 determine the preferred order, that is, the larger the ratio(s) are, the more favored is the AABB-AFM configuration[24]. This is verified by the comparison between the ML-NC3 and ML-C3 structures and the enlarged ratios in the reinforced AABB-AFM state under tensile strain (Tables VII and VIII).

In summary, we exploited four multiferroic phases of NiI_2 from bulk to the ML limit. Their magnetic groundstates are Spiral-B, Spiral-VII^Y, Spiral-V^X, Spiral-IV^X, and AABB-AFM. Those magnetic spirals induce in-plane electric polarizations through the inverse D-M interaction. Thus, ML NiI_2 is a type-II multiferroic material with multiferroicity between AABB-AFM+AFE and Spiral-IV^X + FE tunable by structural details. These fruitful variations arise from competitions among layer-

dependent Heisenberg (an)isotropic exchanges, biquadratic and Kitaev interactions, and single-ion anisotropy. While anisotropic and Kitaev interactions and single-ion anisotropy play a paramount role in the bulk limit [24], the competing Heisenberg exchanges and biquadratic interaction dominate the groundstates in the ML limit. Our results highlight the importance of the layer thickness and geometry in exploring the multiferroic properties of vdW layers down to the ML limit, although the properties causing variation in magnetic interactions require further understanding.

ACKNOWLEDGMENTS

We thank Profs. Hongxin Yang at Nanjing University, Shiwei Wu at Fudan University, and Mingxing Chen at Hunan Normal University for valuable discussions. We gratefully acknowledge financial support from the Ministry of Science and Technology (MOST) of China (Grants No. 2018YFE0202700 and 2023YFA1406500), the National Natural Science Foundation of China (Grants No. 11974422 and 12204534), the Strategic Priority Research Program of the Chinese Academy of Sciences (Grant No. XDB30000000), the Fundamental Research Funds for the Central Universities, and Research Funds of Renmin University of China (Grants No. 22XNKJ30). N.L. is grateful to the China Postdoctoral Science Foundation (2022M713447) for partial financial support. All calculations for this study were performed at the Physics Lab of High-Performance Computing (PLHPC) and the Public Computing Cloud (PCC) of Renmin University of China.

APPENDIX A: SUPPLEMENTARY METHODS

Density functional theory (DFT) calculations were performed using the generalized gradient approximation (GGA) for the exchange–correlation potential, the projector augmented wave (PAW) method [44, 45], and a plane-wave basis set as implemented in the Vienna *ab initio* simulation package (VASP) [46, 47]. A kinetic energy cutoff of 700 (650) eV for the plane waves was used for structural optimization (calculations on the relative energies). A vacuum layer over 20 Å in thickness in the z direction was adopted to eliminate interactions among image layers. The on-site Coulomb interaction was considered with a U value of 4.2 eV and a J value of 0.8 eV for Ni $3d$ orbitals, according to the literature [12, 48] and our energy test calculations of a non-collinear (NCL) and four collinear (CL) magnetic configurations (Fig. 6 in Appendix-B). Spin–orbit coupling (SOC) was considered in all total energy calculations. We used the ferromagnetic (FM) configuration as a reference for the comparison of the total energies in differently sized supercells. The total energies of the FM configuration only differ by 0.08 meV/Ni, indicating good energy convergence for our calculations. Each spiral magnetic order was modeled using a certain propagation vector q within the first Brillouin zone of a $1 \times \sqrt{3} \times 1$ supercell using the generalized Bloch theorem (gBT) [49]. We also constructed supercells of those spiral orders with lower energies obtained by the gBT along the Y-G-X path in the first Brillouin zone for different layers to verify their relative stabilities under consideration of SOC. The Berry phase method [50] was adopted to evaluate the spiral magnetic order-induced electric polarization. The FM state, showing no electric polarization, was used as the reference state to show the layer dependence of the electric polarization values. The transition barrier for monolayer (ML) NiI₂ from the in-plane antiferroelectric (AFE) phase of the AABB antiferromagnetic (AFM) order to a non-electric phase with C₃ symmetry was calculated using the climbing image nudged elastic band (CINEB) method [51]. All atoms, lattice volumes, and shapes in each supercell were allowed to relax until the residual force on each atom was less than 0.01 eV/Å. Grimme’s semiempirical D3

scheme [52] for dispersion correction was employed to describe the vdW interactions in combination with the Perdew–Burke–Ernzerhof functional (PBE-D3) [53]. This combination achieved accuracy comparable to that of the optB86b-vdW functional for describing geometric properties of layered materials [54] at a lower computational cost.

The nearest-neighbor exchange-coupling tensor for Ni–Ni pairs in the xyz basis is:

$$\mathbf{J}_1^{xyz} = \begin{pmatrix} J_{xx} & 0 & 0 \\ 0 & J_{yy} & J_{yz} \\ 0 & J_{yz} & J_{zz} \end{pmatrix}. \quad (\text{A1})$$

If $J_{yz} \neq 0$, adjacent moments will be non-collinearly coupled and lie in a plane off the xy -plane [29].

The tensor \mathbf{J}_1^{xyz} can be diagonalized in the $\alpha\beta\gamma$ basis shown in Fig. 5a in the main text as

$$\mathbf{J}_1^{\alpha\beta\gamma} = \begin{pmatrix} \lambda_\alpha & 0 & 0 \\ 0 & \lambda_\beta & 0 \\ 0 & 0 & \lambda_\gamma \end{pmatrix}. \quad (\text{A2})$$

Therefore, the nearest-neighbor exchange-coupling Hamiltonian in such a basis can be written as

$$H_1 = -\frac{1}{2} \sum_{i \neq j} (\lambda_\alpha S_i^\alpha S_j^\alpha + \lambda_\beta S_i^\beta S_j^\beta + \lambda_\gamma S_i^\gamma S_j^\gamma). \quad (\text{A3})$$

For NiI_2 , we assume $\lambda_\alpha = \lambda_\beta$. H_1 then can be expressed as

$$H_1 = -\frac{1}{2} \sum_{i \neq j} (J \mathbf{S}_i \cdot \mathbf{S}_j + K S_i^\gamma S_j^\gamma), \quad (\text{A4})$$

where $J = (\lambda_\alpha + \lambda_\beta)/2$ is the isotropic nearest-exchange coupling in the $\alpha\beta$ -plane and $K = \lambda_\alpha - J$ is the Kitaev anisotropic nearest-exchange coupling parameter.

The calculated \mathbf{J}_1^{xyz} of ML NiI_2 with the C_3 symmetry is

$$\mathbf{J}_1^{xyz} = \begin{pmatrix} 3.67 & 0 & 0 \\ 0 & 4.64 & 0.20 \\ 0 & 0.20 & 3.68 \end{pmatrix} \quad (\text{A5})$$

and thus

$$\mathbf{J}_1^{\alpha\beta\gamma} = \begin{pmatrix} 3.74 & 0 & 0 \\ 0 & 3.74 & 0 \\ 0 & 0 & 4.51 \end{pmatrix}. \quad (\text{A6})$$

Therefore, $J_{yz} = 0.20$ meV, $J = 3.74$ meV, and $K = 0.77$ meV. The J_{yz} , J , and K

parameters for the other NiI₂ layers can be obtained in a similar way.

APPENDIX B: ENERGY COMPARISONS FOR BULK NiI_2

We considered 5 collinear (Fig. 6) and 55 NCL (Figs. 1e and 1f) magnetic configurations. The experimentally observed spiral order (Spiral-B) shows the lowest energy among these magnetic orders (Fig. 1f and Table I), which is robust regardless of the preservation of the C_3 symmetry (Fig. 1e), consideration of SOC (Fig. 7), and choice of on-site Coulomb interaction (Fig. 8) values.

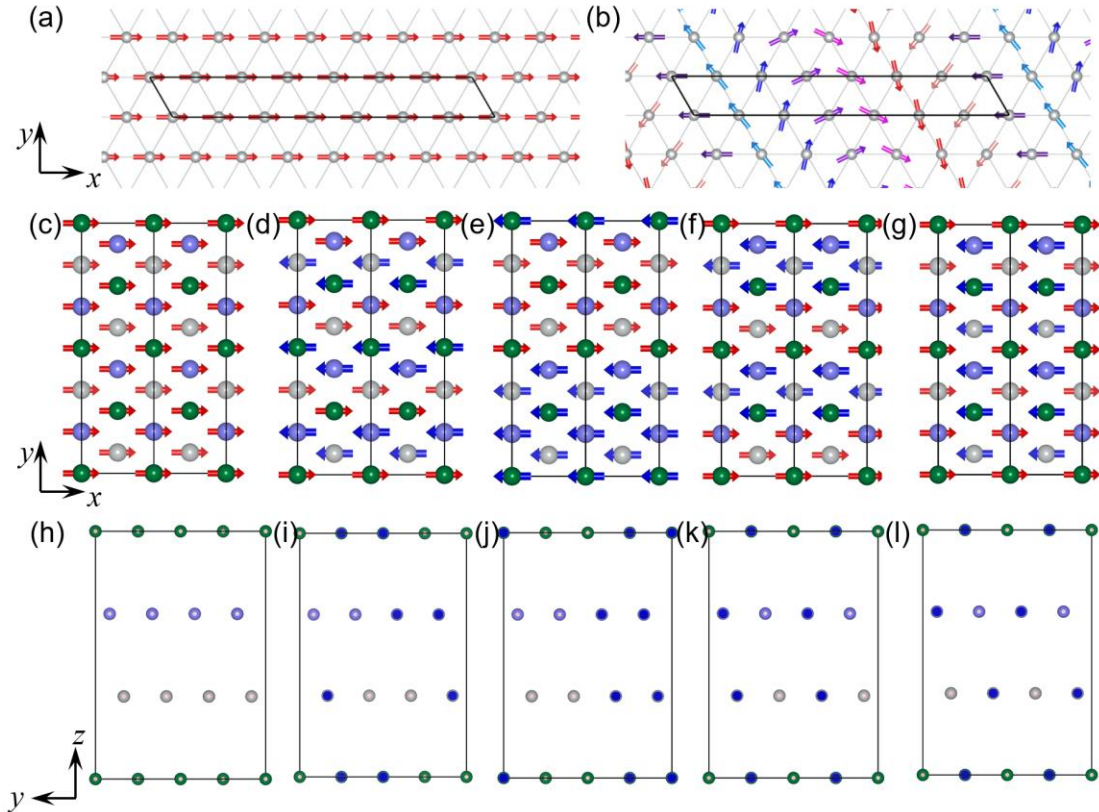


FIG. 6. Schematic models of various collinear and non-collinear (NCL) magnetic configurations for bulk NiI_2 considered in this work, including top views of (a) FM and (b) spiral orders in a $7 \times 1 \times 1$ supercell, and (c) FM, (d) AABB-ABBA-AABB-AFM, (e) AABB-AABB-AABB-AFM, (f) ABAB-ABAB-ABAB-AFM, and (g) AABB-BABA-ABAB-AFM orders in a $1 \times 2\sqrt{3} \times 1$ supercell, with magnetic moments along the x direction. The configuration “AABB-ABBA-AABB-AFM” means AABB-AFM, ABBA-AFM and AABB-AFM magnetic orders in the 1st, 2nd, and 3rd NiI_2 layers, which are labeled by green, grey, and blue balls, respectively. (h-l)

Side views corresponding to (c-g). The black boxes represent different supercells.
Directions of magnetic moments were labeled by colored arrows.

TABLE I. Relative energies (ΔE) of bulk NiI_2 in various collinear and NCL magnetic configurations (shown in Fig. 6). The energy of the Spiral-B [$q_B = (0, 0.138, 1.457)$] order was set to the reference zero. The values in parentheses represent the cases without the C_3 symmetry. Lattice $m \times n$ indicates the number of supercells in the a and b directions. Spiral-B is the magnetic groundstate of bulk NiI_2 .

Lattice	Mag. Config.	ΔE (meV/Ni)
$4 \times \sqrt{3}$	$q_{\text{IV}}^X = (0.250, 0, 0)$	0.64 (0.64)
$5 \times \sqrt{3}$	$q_{\text{V}}^X = (0.200, 0, 0)$	0.19
1×4	$q_{\text{IV}}^Y = (0, 0.250, 0)$	1.91
1×5	$q_{\text{V}}^Y = (0, 0.200, 0)$	0.31
1×6	$q_{\text{VI}}^Y = (0, 0.167, 0)$	0.21
	FM	10.82
1×7	$q_{\text{VII}}^Y = (0, 0.143, 0)$	0.05
	$q_B = (0, 0.138, 1.457)$	0
1×8	$q_{\text{VIII}}^Y = (0, 0.125, 0)$	0.48
	AABB-AABB-AABB-AFM	1.43 (0.73)
$1 \times 2\sqrt{3}$	AABB-ABBA-BBAA-AFM	1.57
	ABAB-ABAB-ABAB-AFM	18.33
	ABAB-BABA-ABAB-AFM	23.17

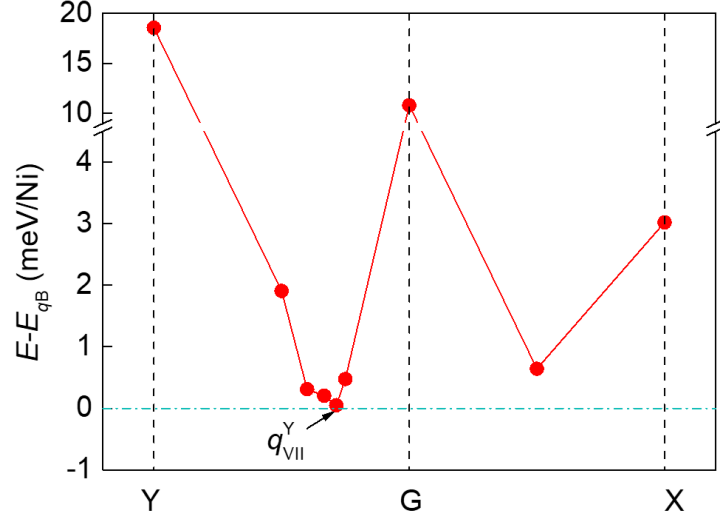


FIG. 7. Energies of various spiral orders along the Y-G-X path in different supercells relative to the total energy of the q_B order (represented by the horizontal dashed cyan line) in bulk NiI_2 . Spin-orbit coupling was considered in all supercells. The comparable order q_{VII}^Y is labeled, which is the in-plane projection of Spiral-B. Spiral-B is the groundstate of bulk NiI_2 .

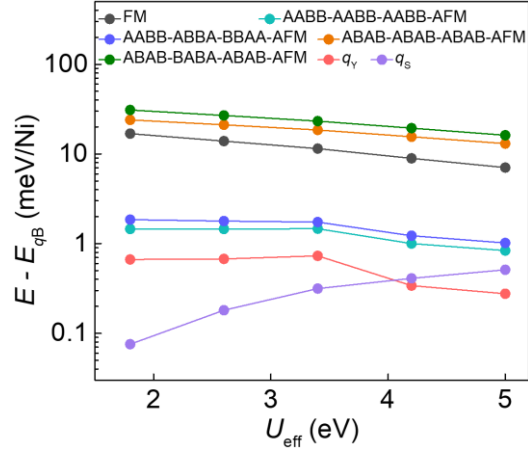


FIG. 8. Effect of different on-site effective Coulomb U values (U_{eff}) on bulk NiI_2 . Comparison of total energies of different magnetic orders relative to that of q_B as a function of U_{eff} values using PBE-D3 functional. The two additional spiral orders are $q_Y = (0, 0.5, 0)$ and $q_S = (0, 0.5, 0.5)$. The Spiral-B ground state of bulk NiI_2 is robust regardless of the choice of U_{eff} values.

APPENDIX C: TOTAL ENERGY COMPARISONS OF VARIOUS MAGNETIC CONFIGURATIONS IN MONOLAYER NiI₂

For monolayer NiI₂, we considered 3 collinear and 19 NCL magnetic orders (Figs. 9 to 13 and Table II) in different supercell sizes (Fig. 9) and a 10×10 q -mesh (Fig. 2a) for the gBT model to explore the magnetic groundstate. Different from the Spiral-B in bulk NiI₂, a new spiral order (Spiral-IV^X) emerges in ML NiI₂ with the C₃ symmetry (ML-C3). The magnetic moments of Spiral-IV^X align in the Ni-I plane (Fig. 10b) and follow a propagating vector $q_{IV}^X = (0.250, 0, 0)$ (across each $4 \times \sqrt{3}$ supercell, Figs. 10a). For the ML NiI₂ without the C₃ symmetry (ML-NC3), the AABB-AFM state is more stable than Spiral-IV^X by 0.35 meV/Ni (Table II). The magnetic groundstate of ML NiI₂ is thus dependent on the structural symmetry, indicating that external strains play a role in modulating their relative stability.

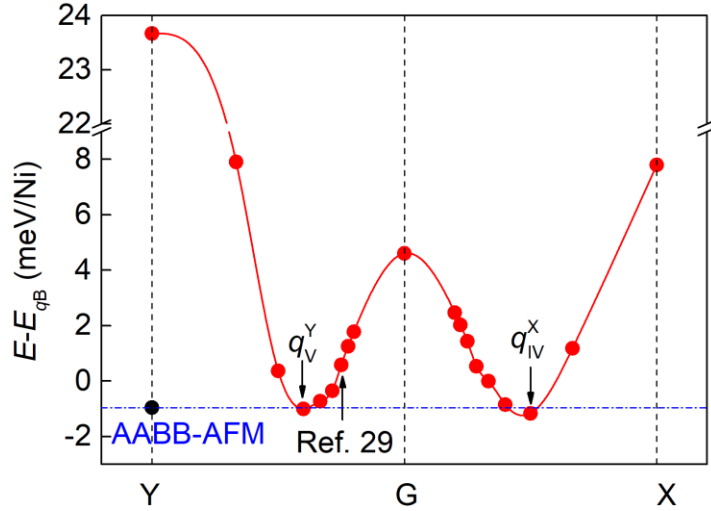


FIG. 9. Comparison of total energies among various spiral orders in different supercells for ML NiI₂ with the C₃ symmetry (ML-C3). The energy of the q_B order was set to the reference zero. Spin-orbit coupling was considered in all supercells. The horizontal dashed blue line represents the energy of AABB-AFM order. The energy of ML NiI₂ in Ref. [29] is also indicated.

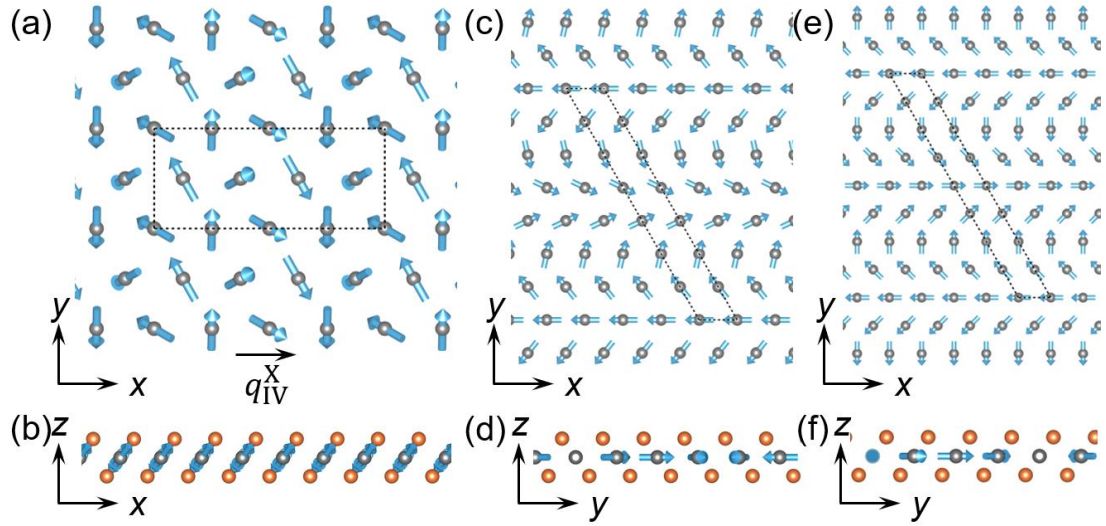


FIG. 10 Schematic plots of spiral orders of ML NiI₂. (a, b) Top and side views of q_{IV}^x with magnetic moments lying in the $\alpha\beta$ -plane (illustrated in Fig. 5a). Spiral orders with propagation vectors along the y direction across (c, d) a 1×7 and (e, f) a 1×8 supercell, the magnetic moments of which lie in the xy -plane.

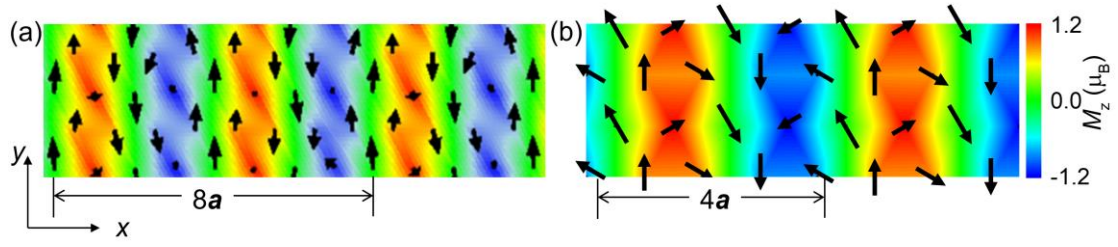


FIG. 11. Magnetic configurations of (a) the spiral order in Fig. 3c of Ref. [11] and (b) Spiral-IV^X. In both figures, black arrows indicate the in-plane components of magnetic moments, while the color maps represent the out-of-plane components. Their propagating vectors of $8a$ and $4a$ were labeled in panels (a) and (b), respectively.

TABLE II. Relative energies ΔE of ML NiI₂ with the C₃ symmetry limitation (ML-C3) in different collinear and NCL magnetic configurations. The energy of q_B order was set to the reference zero. The values in parentheses represent the cases without the C₃ symmetry (ML-NC3). The magnetic ground state of ML-C3 is Spiral-IV^X (q_{IV}^X), while that for ML-NC3 is AABF-AFM order.

Lattice	Mag. Config.	ΔE (meV/Ni)
$2\times\sqrt{3}$	$q_{II}^X = (0.500, 0, 0)$	7.80 (7.34)
$3\times\sqrt{3}$	$q_{IV}^X = (0.333, 0, 0)$	1.19 (0.90)
$4\times\sqrt{3}$	$q_{IV}^X = (0.250, 0, 0)$	-1.16 (-1.33)
$5\times\sqrt{3}$	$q_V^X = (0.200, 0, 0)$	-0.84 (-0.93)
$6\times\sqrt{3}$	$q_{VI}^X = (0.167, 0, 0)$	0.01 (-0.05)
$7\times\sqrt{3}$	$q_{VII}^X = (0.143, 0, 0)$	0.54 (0.51)
$8\times\sqrt{3}$	$q_{VIII}^X = (0.125, 0, 0)$	1.44 (1.42)
1×2	$q_{II}^Y = (0, 0.500, 0)$	23.67 (19.50)
1×3	$q_{III}^Y = (0, 0.333, 0)$	7.91 (8.04)
1×4	$q_{IV}^Y = (0, 0.250, 0)$	-0.37 (0.38)
1×5	$q_V^Y = (0, 0.200, 0)$	-1.00 (-1.04)
1×6	$q_{VI}^Y = (0, 0.167, 0)$	-0.72 (-0.77)
	FM	4.61 (5.37)
1×7	$q_{VII}^Y = (0, 0.143, 0)$	-0.35 (-0.38)
	$q_B = (0, 0.138, 1.457)$	0 (-0.15)
1×8	$q_{VIII}^Y = (0, 0.125, 0)$	0.59 (0.55)
3×2	NCL	15.23
3×3	NCL	8.35
$\sqrt{3}\times\sqrt{3}$	NCL	8.82
$2\sqrt{3}\times\sqrt{3}$	NCL	4.10
$1\times 2\sqrt{3}$	AABF-AFM	-0.95 (-1.68)
	ABAB-AFM	19.46 (24.17)

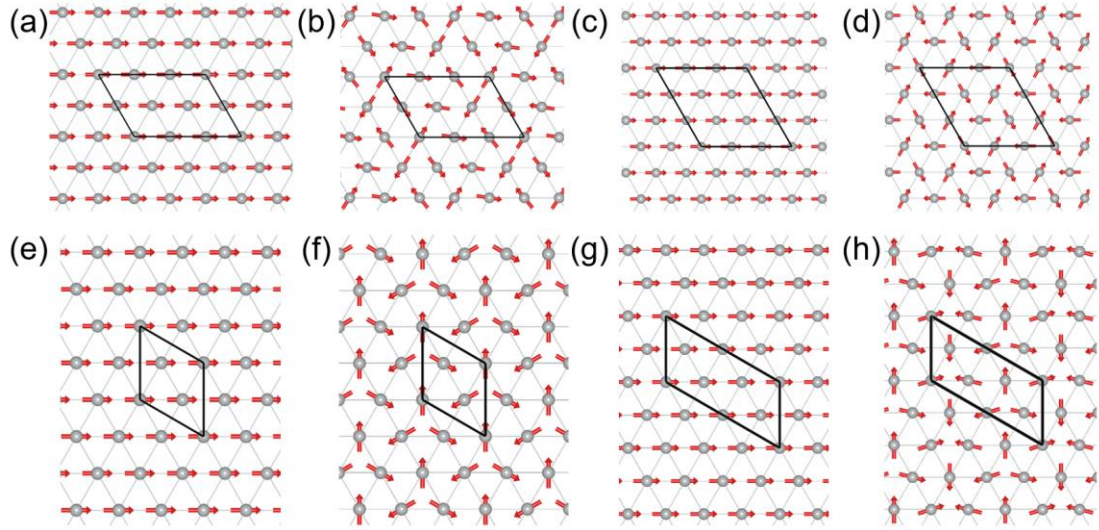


FIG. 12. Schematic plots of collinear and NCL magnetic configurations for ML NiL₂ considered in this work, including (a) FM and (b) NCL in a 3×2 supercell, (c) FM and (d) NCL in a 3×3 supercell, (e) FM and (f) NCL in a $\sqrt{3} \times \sqrt{3}$ supercell, and (g) FM and (h) NCL in a $2\sqrt{3} \times \sqrt{3}$ supercell. The black boxes represent different supercells. Directions of magnetic moments were indicated by red arrows.

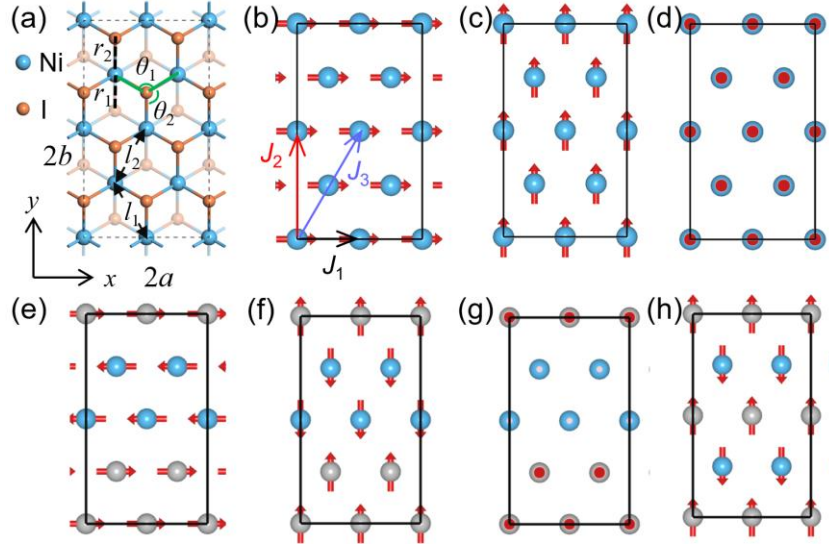


FIG. 13. (a) Structural details of ML NiI_2 . The black rectangle illustrates the $2 \times 2\sqrt{3}$ supercell. The blue and orange spheres indicate Ni and I atoms, respectively. Several key structural parameters, including r_1 , r_2 , θ_1 , θ_2 , l_1 , and l_2 , were marked. Different collinear magnetic configurations with magnetic moments along the x , y , and z directions were shown, including (b) FM order along the x direction, (c) along the y direction, (d) along the z direction, (e) AABF-AFM order along the x direction, (f) along the y direction, (g) along the z direction, and (h) ABAB-AFM order along the y direction.

APPENDIX D: STRAIN EFFECTS ON THE MAGNETIC GROUNDSTATE OF ML NiI₂

We also carried out calculations to compare the stability of some competing magnetic configurations under strains. Configurations q_V^Y and q_{VII}^Y were compared with q_{IV}^X and AABB-AFM under x - y epitaxial strains for NiI₂ MLs without (ML-NC3) and the AABB-AFM configuration was also examined under biaxial strains for ML NiI₂ with the C₃ symmetry (ML-C3). Figure 14a clearly illustrates that either the AABB-AFM or the Spiral-IV^X order exhibits the best stability among all four considered magnetic orders. In particular, Spiral-IV^X (red plane) is always more stable than q_V^Y (by 0.12 to 0.41 meV/Ni, yellow plane in Fig. 14a), q_{VII}^Y (by 0.42 to 1.67 meV/Ni, green plane in Fig. 14a) in ML-NC3, and AABB-AFM in ML-C3 (AABB-C3, by 0.14 to 0.31 meV/Ni, Fig. 14b) in the whole considered strain range. In certain strain regions, the AABB-AFM order (blue plane in Fig. 14a) becomes more stable than Spiral-IV^X. Based on these results, we verified the reliability of only comparing the energies of q_{IV}^X and AABB-AFM for competing the magnetic ground state of ML NiI₂.

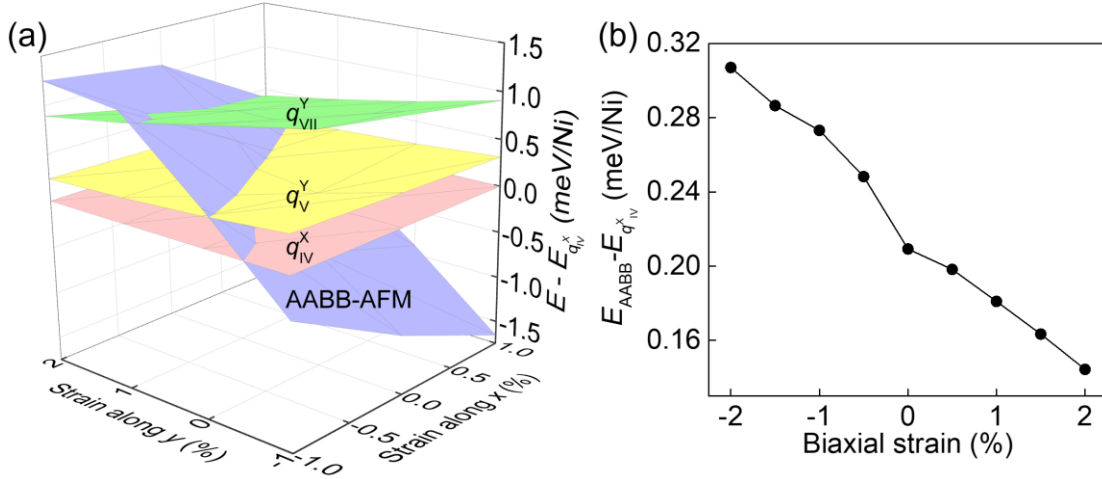


FIG. 14. (a) Relative energies of Spiral-V^Y (q_V^Y), Spiral-VII^Y (q_{VII}^Y), and AABB-AFM to that of Spiral-IV^X (q_{IV}^X) for ML-NC3 under epitaxial strains along the x and y directions. (b) Relative energy of AABB-AFM to q_{IV}^X for ML-C3 as a function of biaxial strains.

APPENDIX E: LAYER-DEPENDENT MAGNETIC GROUNDSTATES FOR FEWLAYERS NiI₂

For constrain-free 2L NiI₂, the AABB-AFM order is less stable than other NCL orders (Table III). A new spiral order, named Spiral-V^X emerges and is 0.26 meV/Ni more stable than Spiral-IV^X. The magnetic moments of Spiral-V^X propagate along the x direction and across each $5 \times \sqrt{3}$ supercell. Spiral-V^X is also more stable than Spiral-VII^Y and Spiral-B by 0.24 and 0.18 meV/Ni, nearly energetically undistinguishable. The Spiral-VII^Y is the in-plane projection of Spiral-B and propagates along the y direction across a 1×7 supercell. Breakdown or preservation of the C₃ symmetry doesn't change the relative stability of these spiral orders (Table III). For 3L NiI₂, Spiral-VII^Y and Spiral-B are still energetically degenerated, but over 0.35 meV/Ni more stable than Spiral-IV^X and Spiral-V^X (TABLE IV). For 4L and thicker NiI₂, Spiral-B becomes the most stable among various collinear and NCL magnetic configurations (Table V).

TABLE III. Relative energies ΔE of bilayer (2L) NiI₂ with the C₃ symmetry limitation (2L-C3) in different collinear and NCL magnetic configurations. The energy of q_B order was set to reference zero. The values in parentheses represent the cases without the C₃ symmetry (2L-NC3).

Lattice	Mag. Config.	ΔE (meV/Ni)
$4 \times \sqrt{3}$	$q_{IV}^X = (0.250, 0, 0)$	0.08 (0.02)
$5 \times \sqrt{3}$	$q_V^X = (0.200, 0, 0)$	-0.18 (-0.08)
$6 \times \sqrt{3}$	$q_{VI}^X = (0.167, 0, 0)$	0.27 (0.28)
$7 \times \sqrt{3}$	$q_{VII}^X = (0.143, 0, 0)$	0.42 (0.39)
1×4	$q_{IV}^Y = (0, 0.250, 0)$	1.63
1×5	$q_V^Y = (0, 0.200, 0)$	-0.03 (0.14)
1×6	$q_{VI}^Y = (0, 0.167, 0)$	0.11
1×7	FM	8.11 (8.48)

	$q_{\text{VII}}^{\text{Y}} = (0, 0.143, 0)$	0.06 (-0.01)
	$q_{\text{B}} = (0, 0.138, 1.457)$	0 (-0.02)
1×8	$q_{\text{VIII}}^{\text{Y}} = (0, 0.125, 0)$	0.64
$1 \times 2\sqrt{3}$	AABB-AABB-AFM	0.56 (0.27)
	AABB-ABBA-AFM	1.03 (0.62)

TABLE IV. Relative energies ΔE of trilayer (3L) NiI₂ with the C₃ symmetry limitation (3L-C3) in different collinear and NCL magnetic configurations. The energy of q_B order was set to reference zero. The values in parentheses represent the cases without the C₃ symmetry (3L-NC3).

Lattice	Mag. Config.	ΔE (meV/Ni)
$4 \times \sqrt{3}$	$q_{IV}^X = (0.250, 0, 0)$	0.65 (0.90)
$5 \times \sqrt{3}$	$q_V^X = (0.200, 0, 0)$	0.35
$6 \times \sqrt{3}$	$q_{VI}^X = (0.167, 0, 0)$	0.50
1×4	$q_{IV}^Y = (0, 0.250, 0)$	2.19
1×5	$q_V^Y = (0, 0.200, 0)$	0.44
1×6	$q_{VI}^Y = (0, 0.167, 0)$	0.20
	FM	9.44
1×7	$q_{VII}^Y = (0, 0.143, 0)$	0.06
	$q_B = (0, 0.138, 1.457)$	0
1×8	$q_{VIII}^Y = (0, 0.125, 0)$	0.61
	AABB-AABB-AABB-AFM	1.17 (0.45)
$1 \times 2\sqrt{3}$	AABB-ABBA-BBAA-AFM	1.84
	ABAB-ABAB-ABAB-AFM	18.01
	ABAB-BABA-ABAB-AFM	22.76

TABLE V. Relative energies ΔE of four-layer (4L) NiI_2 with the C_3 symmetry limitation (4L-C3) in different collinear and NCL magnetic configurations. The energy of q_B order was set to reference zero. The values in parentheses represent the cases without the C_3 symmetry (4L-NC3).

Lattice	Mag. Config.	ΔE (meV/Ni)
$4 \times \sqrt{3}$	$q_{IV}^X = (0.250, 0, 0)$	0.86 (0.70)
$5 \times \sqrt{3}$	$q_V^X = (0.200, 0, 0)$	0.52
$6 \times \sqrt{3}$	$q_{VI}^X = (0.167, 0, 0)$	0.57
1×4	$q_{IV}^Y = (0, 0.250, 0)$	2.40
1×5	$q_V^Y = (0, 0.200, 0)$	1.28
1×6	$q_{VI}^Y = (0, 0.167, 0)$	0.30
	FM	10.15
1×7	$q_{VII}^Y = (0, 0.143, 0)$	0.14
	$q_B = (0, 0.138, 1.457)$	0
1×8	$q_{VIII} = (0, 0.125, 0)$	0.64
	AABB-AABB-AABB-AABB-AFM	1.44 (0.70)
	AABB-AABB-ABBA-ABBA-AFM	1.69
$1 \times 2\sqrt{3}$	AABB-ABBA-ABBA-AABB-AFM	1.55
	AABB-AABB-AABB-ABBA-AFM	1.69
	ABBA-ABBA-ABBA-AABB-AFM	1.31

APPENDIX F: EFFECTS OF DIFFERENT U_{eff} VALUES AND FUNCTIONALS ON THE MAGNETIC STABILITY OF ML NiI₂

We examined the effect of on-site effect U_{eff} values and functionals on the magnetic groundstate of ML NiI₂. As shown in Fig. 15a, for ML-NC3 (ML-C3), the AABB-AFM (q_{IV}^{X}) state always shows the lowest energy under different U_{eff} values and functionals (orange squares). The relative stability for these magnetic configurations was also checked using the HSE06 functional (Fig. 15b).

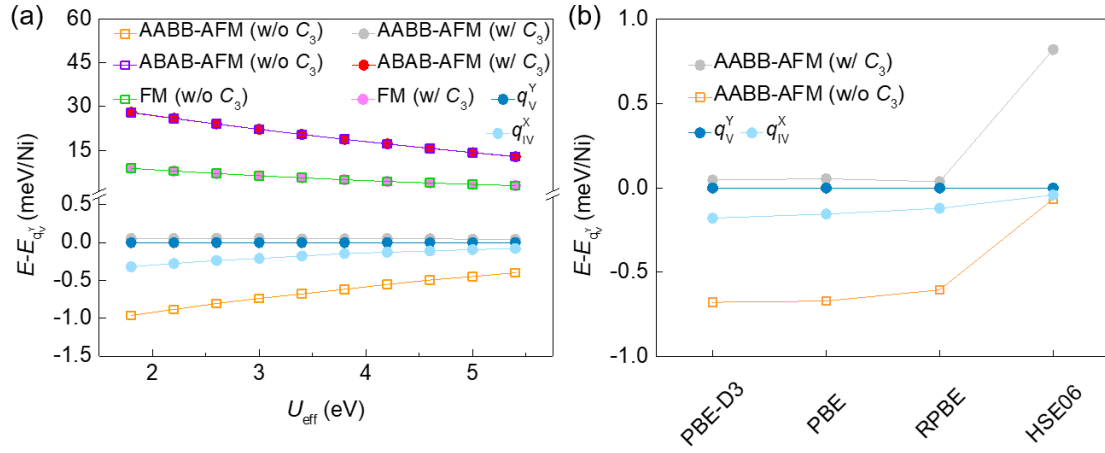


FIG. 15. Total energies of different magnetic orders to that of the Spiral- V^Y state were shown as functions of (a) effective U_{eff} values using PBE-D3 functional and (b) functionals with $U_{\text{eff}} = 3.8$ eV. Spin-orbit coupling was considered in the PBE-D3, PBE, and RPBE functionals. U_{eff} was not used for the HSE06 functional calculation.

APPENDIX G: ELECTRIC PROPERTIES FOR ML NiI₂ WITH AND WITHOUT THE C₃ SYMMETRY

We used the NEB method to calculate the energy barriers for the spin canting process of ML-C3 from q_{IV}^X to $-q_{IV}^X$ (Fig. 16a) and AFE transition of ML-NC3 through a non-electric phase (Fig. 16b). As listed in Table VI, the lattice b shrinks for the AABB-AFM state relative to that of FM order. In the AABB-AFM order, the Ni atoms in the same AFM stripe move oppositely by 0.004 Å in the $\pm y$ directions, yielding a dipole moment of ± 1.5 pC/m (Fig. 3g).

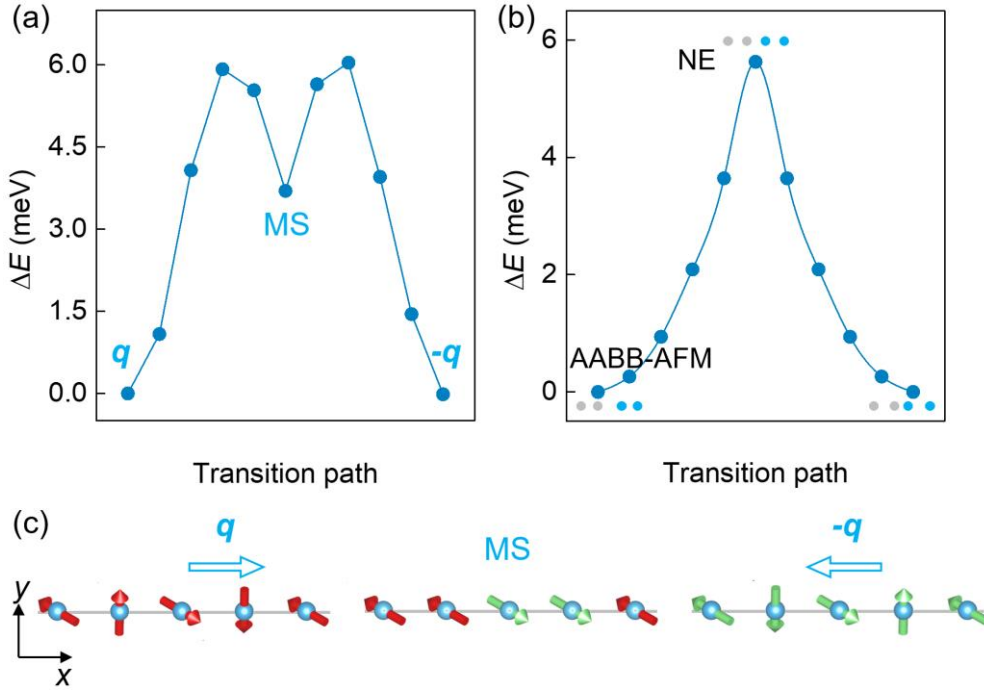


FIG. 16. (a) Calculated energy barrier for the spin canting process of ML NiI₂, taking Spiral-IV^X order (illustrated in Figs. 3a-3c). (b) Transition pathway for ML NiI₂ between the two AFE phases through a non-electric (NE) phase. The insets blue and gray circles represent the Ni atoms in different magnetic stripes. (c) Initial, metastable (MS) and final magnetic configurations for the spin canting process in (a).

TABLE VI. Structural details of ML NiI₂ in a $2 \times 2\sqrt{3}$ supercell with different magnetic configurations (marked in Fig. 13a). Sym. represents the space point group symmetry.

Spin config.	$2a$ (Å)	$2\sqrt{3}b$ (Å)	l_1 (Å)	l_2 (Å)	θ_1 (°)	θ_2 (°)	Sym.
FM	7.86	13.61	3.93	3.93	91.21	91.21	$\bar{P}3m1$
AABB-AFM	7.85	13.56	3.91	3.93	90.98	91.15	P21/ <i>m</i>
ABAB-AFM	7.86	13.61	3.93	3.93	91.18	91.18	P21/ <i>m</i>
ZZ-AFM	7.87	13.63	3.91	3.93	90.95	91.13	P2/C

APPENDIX H: SUBSTRATE EFFECT ON MAGNETIC GROUNDSTATE OF ML NiI₂

The relation between lattices of the ML NiI₂ and hBN substrate is yet to be uncovered in experiments. Without such experimental input, we theoretically constructed the superlattices of their heterostructures using a criterion of optimal lattice mismatching. We adopted the supercell with lattice of -0.6% along the x direction and 1.3% along the y direction (referred to as Str.1), and an alternative hexangular supercell (referred to as Str.2, Fig. 17a) and a rectangular one (referred to as Str.3, Fig. 17b), exhibiting the second and the third smallest lattices mismatches, namely 2.1% along both the x and y directions in Str.2, and 3.8% along the x directions and -4.0% along the y direction in Str.3. Please be aware that the strains in Str.2 are in the tensile region, while the $x(y)$ -strain in Str.3 is in the opposite direction of that for Str.1, namely tensile (compressive) $x(y)$ -strain. Our calculations indicate that Str.1 is 1.43 and 2.48 meV/Ni more stable than Str.2 and Str.3, respectively, given a defined interfacial binding energy $E_b = E_{\text{tot}} - E_{\text{hBN}} - E_{\text{NiI}_2}$, where E_{tot} , E_{hBN} and E_{NiI_2} denote the energies of the heterostructure, hBN and NiI₂, respectively.

In Str.1, the Ni layer (Fig. 18a) and the two I sublayers (Fig. 19) exhibit out-of-plane corrugations varying up to 0.06 Å. In-plane strains break the inversion symmetry in the x (Fig. 18c) and y (Fig. 18d) directions. Moreover, explicit interfacial charge transfer from the hBN substrate to the interfacial I layer leads to an out-of-plane electric polarization (Figs. 18e and 18f).

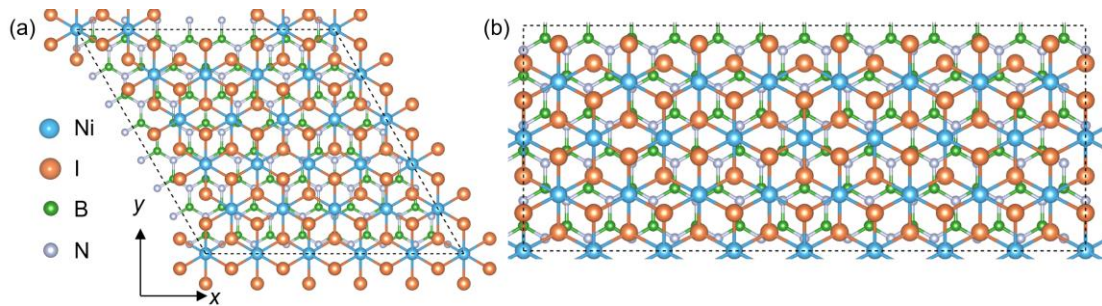


FIG. 17. Top view of two alternative NiI₂/hBN heterostructures in the tensile strain region, exhibiting lattice mismatches of 2.1% for the x and y directions in (a) and 3.8%

along the x direction and -4.0% along the y direction in (b). The hexangular and rectangular supercells are depicted, highlighting the relative arrangement of the layers.

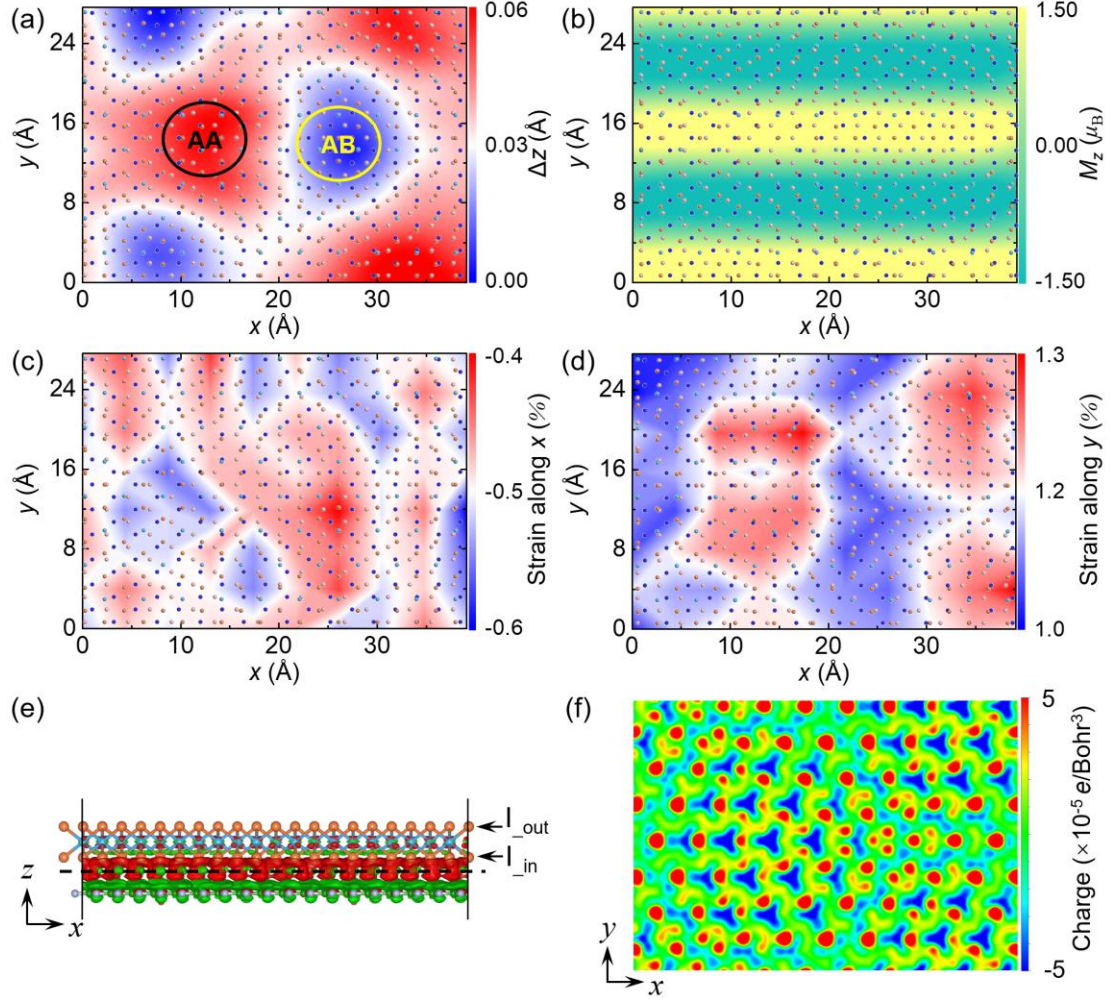


FIG. 18. Structure and magnetism of the epitaxial ML Ni₂ on a *h*BN substrate, including 2D mappings of the variation in (a) the *z* coordinates and (b) the magnetic moments of Ni atoms in the heterostructure taking the AABF-AFM state, and in-plane strains along the (c) *x* and (d) *y* directions. (e) Side view of differential charge density and (f) 2D profile maps along the dashed lines in (e) with an isosurface value of $5 \times 10^{-5} e/\text{Bohr}^3$. The red and green contours in (e) and (f) are charge accumulation and depletion, respectively. The lower and upper I atoms of ML Ni₂ on *h*BN are labeled by I_{in} and I_{out} in (e).

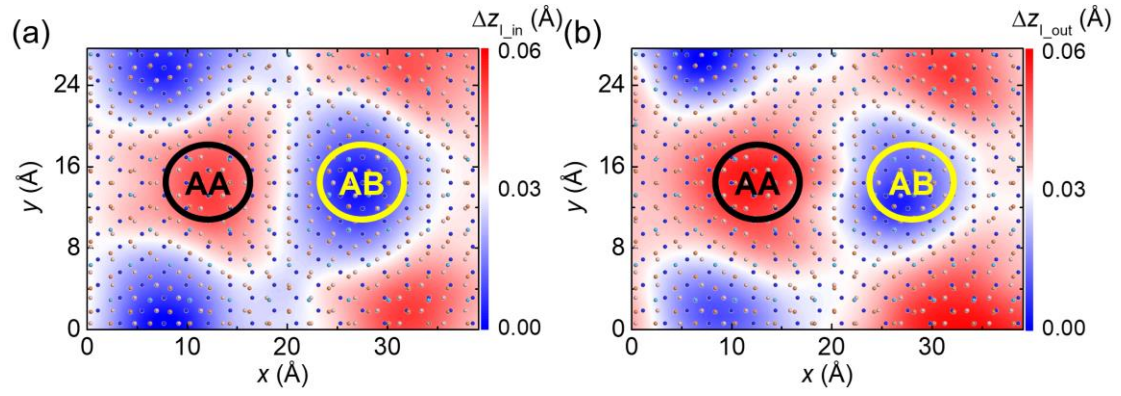


FIG. 19. Two-dimensional mappings of the z -coordinates of the (a) I_{in} and (b) I_{out} atoms (labeled in Fig. 18e) of ML NiI_2 adsorbed on the hBN substrate. The spatial variations for z -coordinates of the I_{in} and I_{out} indicate out-of-plane inversion symmetry breaking for NiI_2 on hBN substrate.

APPENDIX I: EFFECT OF ELECTRON DOPING ON THE RELATIVE STABILITY BETWEEN SPIRAL-IV^X AND AABB-AFM ORDERS

We considered the effect of electron doping on the relative stability between AABB-AFM and Spiral-IV^X for the both structures. As shown in Fig. 20, for ML-C3, the Spiral-IV^X is always more stable than the AABB-AFM (red dots), while it is preferred for doping concentration larger than 0.02 e/I for ML-NC3 (black dots). The hBN substrate interacts strongly with ML Ni₂, the C₃ symmetry of ML Ni₂ thus is, most likely, maintained on hBN. Moreover, electrons are transferred from hBN to ML Ni₂ (Fig. 18e). The magnetic groundstate of ML Ni₂ on hBN is thus the Spiral-IV^X.

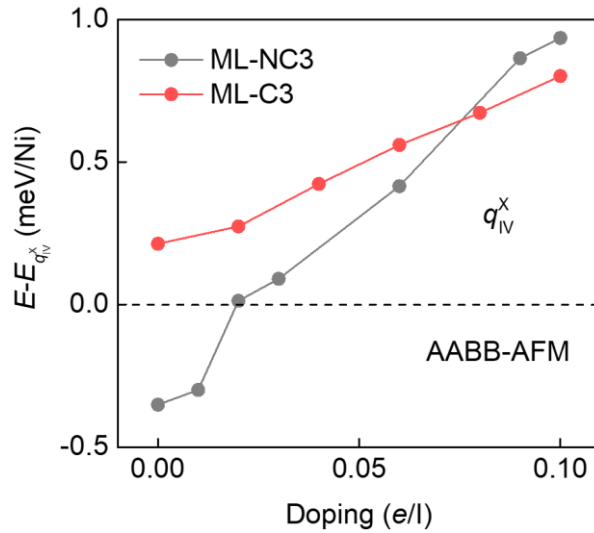


FIG. 20. Energy difference between AABB-AFM and Spiral-IV^X orders for ML-NC3 (black) and ML-C3 (red) under different doping concentrations. For ML-NC3, order Spiral-IV^X is more stable than AABB-AFM order when doping concentration is larger than 0.02 e/I , while it is always more preferred than AABB-AFM order for ML-C3 under electron doping.

APPENDIX J: COMPARISON OF INTERFACIAL INTERACTIONS FOR NiI₂/hBN AND NiI₂/SiO₂ HETEROSTRUCTURES

To more clearly show the different interfacial interactions for ML NiI₂ on hBN and SiO₂ substrates, we performed calculations for a ML NiI₂ on an amorphous SiO₂ substrate. The fully relaxed atomic structure of the NiI₂/SiO₂ interface is shown in Fig. 4a. We plotted line profiles along the z direction of interfacial differential charge density (DCD) variations for both NiI₂/hBN (red line in Fig. 4b) and NiI₂/SiO₂ (blue line in Fig. 4b) interfaces. The NiI₂/BN interface exhibits significant charge variations across the interface while that of the NiI₂/SiO₂ interface is nearly inappreciable, indicating a much weaker interaction of SiO₂ to the NiI₂ monolayer. The weaker interacting SiO₂ also leads to a less-uniformed interfacial structure. As mapped in Fig. 4c, the SiO₂ substrate exhibits a much larger range, namely from 2.88 to 5.24 Å, for the vertical distance between interfacial I and O atoms. However, the range for the hBN substrate is much narrower, namely from 3.63 to 3.70 Å, as depicted in Fig. 4d. The smaller vertical corrugation of the NiI₂/hBN interface also gives rise to an averaged interfacial distance of 3.67 Å, 0.39 Å smaller than that of the NiI₂/SiO₂ interface (4.06 Å). Therefore, these results indicate that the amorphous SiO₂ substrate, most likely, interacts with the NiI₂ ML more weakly than the hBN substrate, which means the SiO₂ substrate is less capable of efficiently applying in-plane strain confinements to the NiI₂ ML. In other words, the hBN substrate may have a chance to force the NiI₂ ML following the C₃ symmetry of the substrate, while the SiO₂ substrate, most likely, cannot.

APPENDIX K: EVOLUTION OF LAYER-DEPENDENT MAGNETIC ANISOTROPIC ENERGY (MAE)

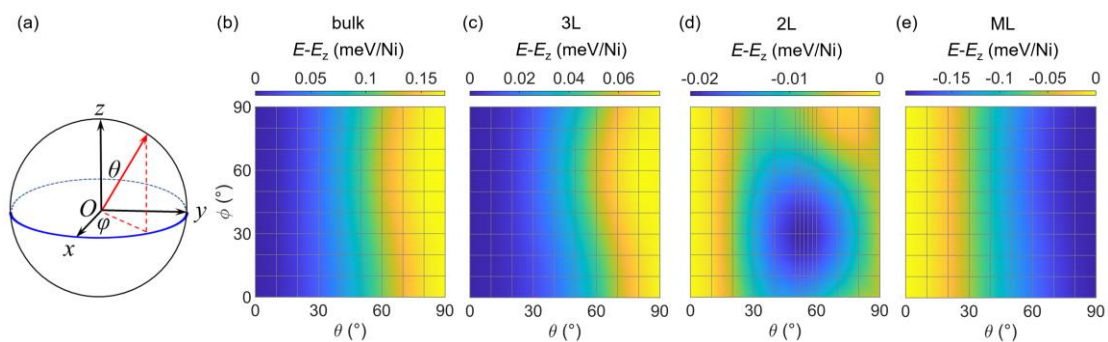


FIG. 21. (a) Illustration of magnetization axes in MAE calculation. Here θ and φ are the angles between the magnetization direction and z and x axes, respectively. Angular dependence energies relative to that of magnetic moment along the z axis for (b) bulk, (c) 3L, (d) 2L and (e) ML NiI₂ taking FM order. From ML to bulk NiI₂, magnetic moments undergo a spin reorientation from in-plane to out-of-plane direction.

APPENDIX L: LAYER-DEPENDENT MAGNETIC PARAMETERS

TABLE VII. Isotropic exchange parameters J_1 , J_2 , and J_3 for the nearest, second nearest, and third nearest Ni atoms, and interlayer isotropic exchange parameters J_1^\perp , J_2^\perp , and J_3^\perp for the nearest, second nearest, and third nearest Ni atoms, their ratios $|J_1/J_3|$ and J_2/J_1 , Kitaev K , single-ion anisotropy A_z , and magnetic dipole interaction over J_1 (B/J_1), and two-site anisotropy over J_1 (J_{yz}/J_1) of NiI₂ with the C₃ symmetry.

	J_1 (meV)	J_2 (meV)	J_3 (meV)	J_1^\perp (meV)	J_2^\perp (meV)	J_3^\perp (meV)	$ J_1/J_3 $	J_2/J_1	K (meV)	A_z (meV)	B/J_1	J_{yz}/J_1
ML	3.89	-0.25	-3.09	--	--	--	1.26	-0.06	0.77	1.43	0.24	0.05
2L	3.55	0.17	-3.29	0.37	-1.52	-0.28	1.08	0.05	2.41	1.55	0.34	0.44
3L	3.36	0.07	-3.06	0.04	-1.29	-0.23	1.10	0.02	2.42	1.58	0.37	0.49
4L	3.32	0.08	-3.04	0.08	-1.32	-0.24	1.09	0.03	2.42	1.59	0.40	0.52
bulk	3.22	0.29	-3.48	0.49	-2.05	-0.38	0.92	0.09	2.44	1.60	0.44	0.58

TABLE VIII. Isotropic exchange parameters J_1 , J_2 , J_3 , J_1^\perp , J_2^\perp , and J_3^\perp , and their ratios $|J_1/J_3|$ and J_2/J_1 , K , A_z , B/J_1 and J_{yz}/J_1 of NiI₂ without the C₃ symmetry. The “Strained ML” refers to ML-NC3 undergoing a tensile strain of 1.0 % along the x direction (Strained ML).

	J_1 (meV)	J_2 (meV)	J_3 (meV)	J_1^\perp (meV)	J_2^\perp (meV)	J_3^\perp (meV)	$ J_1/J_3 $	J_2/J_1	K (meV)	A_z (meV)	B/J_1	J_{yz}/J_1
ML	3.92	-0.26	-3.20	--	--	--	1.22	-0.07	0.77	1.43	0.24	0.05
Strained ML	3.97	-0.34	-3.49	--	--	--	1.23	-0.09	1.73	1.45	0.29	0.25
2L	3.59	0.12	-3.40	0.38	-1.53	-0.28	1.06	0.03	2.41	1.55	0.34	0.44
3L	3.29	0.13	-3.14	0.05	-1.31	-0.24	1.05	0.04	2.42	1.58	0.37	0.49
4L	3.36	0.03	-3.17	0.10	-1.34	-0.25	1.06	0.01	2.42	1.59	0.40	0.52
bulk	3.27	0.24	-3.61	0.50	-2.05	-0.40	0.91	0.07	2.44	1.60	0.44	0.58

References

- [1] N.A. Spaldin and R. Ramesh, Advances in magnetoelectric multiferroics, *Nat. Mater.* **18**, 203 (2019).
- [2] T. Kimura, T. Goto, H. Shintani, K. Ishizaka, T. Arima, and Y. Tokura, Magnetic control of ferroelectric polarization, *Nature* **426**, 55 (2003).
- [3] N. Terada, D.D. Khalyavin, P. Manuel, F. Orlandi, C.J. Ridley, C.L. Bull, R. Ono, I. Solovyev, T. Naka, D. Prabhakaran, and A.T. Boothroyd, Room-Temperature Type-II Multiferroic Phase Induced by Pressure in Cupric Oxide, *Phys. Rev. Lett.* **129**, 217601 (2022).
- [4] N.A. Spaldin, Multiferroics: from the cosmically large to the subatomically small, *Nat. Rev. Mater.* **2**, 17017 (2017).
- [5] M. Fiebig, T. Lottermoser, D. Meier, and M. Trassin, The evolution of multiferroics, *Nat. Rev. Mater.* **1**, 16046 (2016).
- [6] S. Dong, H. Xiang, and E. Dagotto, Magnetoelectricity in multiferroics: a theoretical perspective, *Natl. Sci. Rev.* **6**, 629 (2019).
- [7] S. Dong, J.-M. Liu, S.-W. Cheong, and Z. Ren, Multiferroic materials and magnetoelectric physics: symmetry, entanglement, excitation, and topology, *Adv. Phys.* **64**, 519 (2015).
- [8] T. Kurumaji, S. Seki, S. Ishiwata, H. Murakawa, Y. Kaneko, and Y. Tokura, Magnetoelectric responses induced by domain rearrangement and spin structural change in triangular-lattice helimagnets NiI₂ and CoI₂, *Phys. Rev. B* **87**, 014429 (2013).
- [9] H. Liu, X. Wang, J. Wu, Y. Chen, J. Wan, R. Wen, J. Yang, Y. Liu, Z. Song, and L. Xie, Vapor Deposition of Magnetic Van der Waals NiI₂ Crystals, *ACS Nano* **14**, 10544 (2020).
- [10] H. Ju, Y. Lee, K.-T. Kim, I.H. Choi, C.J. Roh, S. Son, P. Park, J.H. Kim, T.S. Jung, J.H. Kim, K.H. Kim, J.-G. Park, and J.S. Lee, Possible Persistence of Multiferroic Order down to Bilayer Limit of van der Waals Material NiI₂, *Nano Lett.* **21**, 5126 (2021).
- [11] Q. Song, C.A. Occhialini, E. Ergecen, B. Ilyas, D. Amoroso, P. Barone, J. Kapteghian, K. Watanabe, T. Taniguchi, A.S. Botana, S. Picozzi, N. Gedik, and R. Comin, Evidence for a single-layer van der Waals multiferroic, *Nature* **602**, 601 (2022).
- [12] A.S. Botana and M.R. Norman, Electronic structure and magnetism of transition metal dihalides: Bulk to monolayer, *Phys. Rev. Mater.* **3**, 044001 (2019).
- [13] M. Lu, Q. Yao, C. Xiao, C. Huang, and E. Kan, Mechanical, Electronic, and Magnetic Properties of NiX₂ (X = Cl, Br, I) Layers, *ACS Omega* **4**, 5714 (2019).
- [14] V.V. Kulish and W. Huang, Single-layer metal halides MX₂ (X = Cl, Br, I): stability and tunable magnetism from first principles and Monte Carlo simulations, *J. Mater. Chem. C* **5**, 8734 (2017).
- [15] A.O. Fumega and J.L. Lado, Microscopic origin of multiferroic order in monolayer NiI₂, *2D Materials* **9**, 025010 (2022).
- [16] J. Sødquist and T. Olsen, Type II multiferroic order in two-dimensional transition metal halides from first principles spin-spiral calculations, *2D Mater.* **10**, 035016 (2023).
- [17] J.Y. Ni, X.Y. Li, D. Amoroso, X. He, J.S. Feng, E.J. Kan, S. Picozzi, and H.J. Xiang, Giant Biquadratic Exchange in 2D Magnets and Its Role in Stabilizing Ferromagnetism of NiCl₂ Monolayers, *Phys. Rev. Lett.* **127**, 247204 (2021).
- [18] C. Xu, J. Feng, M. Kawamura, Y. Yamaji, Y. Nahas, S. Prokhorenko, Y. Qi, H. Xiang, and L. Bellaïche, Possible Kitaev Quantum Spin Liquid State in 2D Materials with $S=3/2$,

- Phys. Rev. Lett. **124**, 087205 (2020).
- [19]C. Xu, J. Feng, H. Xiang, and L. Bellaiche, Interplay between Kitaev interaction and single ion anisotropy in ferromagnetic CrI₃ and CrGeTe₃ monolayers, NPJ Comput. Mater. **4**, 57 (2018).
- [20]N. Liu, S. Zhou, and J. Zhao, High-Curie-temperature ferromagnetism in bilayer CrI₃ on bulk semiconducting substrates, Phys. Rev. Mater. **4**, 094003 (2020).
- [21]L. Wu, L. Zhou, X. Zhou, C. Wang, and W. Ji, In-plane epitaxy-strain-tuning intralayer and interlayer magnetic coupling in CrSe₂ and CrTe₂ monolayers and bilayers, Phys. Rev. B **106**, L081401 (2022).
- [22]S.R. Kuindersma, J.P. Sanchez, and C. Haas, Magnetic and Structural Investigations on NiI₂ and CoI₂, Physica B & C **111**, 231 (1981).
- [23]H. Ju, Y. Lee, K.T. Kim, I.H. Choi, C.J. Roh, S. Son, P. Park, J.H. Kim, T.S. Jung, J.H. Kim, K.H. Kim, J.G. Park, and J.S. Lee, Possible Persistence of Multiferroic Order down to Bilayer Limit of van der Waals Material NiI₂, Nano Lett. **21**, 5126 (2021).
- [24]X. Li, C. Xu, B. Liu, X. Li, L. Bellaiche, and H. Xiang, Realistic Spin Model for Multiferroic NiI₂, Phys. Rev. Lett. **131**, 036701 (2023).
- [25]S. Paul, R. Torsi, J.A. Robinson, and K. Momeni, Effect of the Substrate on MoS₂ Monolayer Morphology: An Integrated Computational and Experimental Study, ACS Appl. Mater. Inter. **14**, 18835 (2022).
- [26]M. Bonilla, S. Kolekar, Y. Ma, H.C. Diaz, V. Kalappattil, R. Das, T. Eggers, H.R. Gutierrez, M.-H. Phan, and M. Batzill, Strong room-temperature ferromagnetism in VSe₂ monolayers on van der Waals substrates, Nat. Nanotechnol. **13**, 289 (2018).
- [27]H. Yu, Z. Yang, L. Du, J. Zhang, J. Shi, W. Chen, P. Chen, M. Liao, J. Zhao, J. Meng, G. Wang, J. Zhu, R. Yang, D. Shi, L. Gu, and G. Zhang, Precisely Aligned Monolayer MoS₂ Epitaxially Grown on h-BN basal Plane, Small **13**, 1603005 (2017).
- [28]B. Li, Z. Wan, C. Wang, P. Chen, B. Huang, X. Cheng, Q. Qian, J. Li, Z.W. Zhang, G.Z. Sun, B. Zhao, H.F. Ma, R.X. Wu, Z.M. Wei, Y. Liu, L. Liao, Y. Ye, Y. Huang, X.D. Xu, X.D. Duan, W. Ji, and X.F. Duan, Van der Waals epitaxial growth of air-stable CrSe₂ nanosheets with thickness-tunable magnetic order, Nat. Mater. **20**, 818 (2021).
- [29]D. Amoroso, P. Barone, and S. Picozzi, Spontaneous skyrmionic lattice from anisotropic symmetric exchange in a Ni-halide monolayer, Nat. Commun. **11**, 5784 (2020).
- [30]S. Wu, X. Chen, C. Hong, X. Hou, Z. Wang, Z. Sheng, Z. Sun, Y. Guo, and S. Wu, Layer thickness crossover of type-II multiferroic magnetism in NiI₂, arXiv preprint arXiv:2307.10686, (2023).
- [31]M.-P. Miao, N. Liu, W.-H. Zhang, D.-B. Wang, W. Ji, and Y.-S. Fu, Spin-resolved imaging of atomic-scale helimagnetism in monolayer NiI₂, arXiv preprint arXiv:2309.16526, (2023).
- [32]X. Ni, Daoxin Yao, and K. Cao, In-plane strain tuning multiferroicity in monolayer van der Waals NiI₂, arXiv:2209.12392, (2022).
- [33]M. Amini, A.O. Fumega, H. González-Herrero, V. Vaño, S. Kezilebieke, J.L. Lado, and P. Liljeroth, Atomic-scale visualization of multiferroicity in monolayer NiI₂, arXiv preprint arXiv:2309.11217, (2023).
- [34]Q. Cui, J. Liang, B. Yang, Z. Wang, P. Li, P. Cui, and H. Yang, Giant enhancement of perpendicular magnetic anisotropy and induced quantum anomalous Hall effect in

- graphene/NiI₂ heterostructures via tuning the van der Waals interlayer distance, *Phys. Rev. B* **101**, 214439 (2020).
- [35]M. Cococcioni and S. de Gironcoli, Linear response approach to the calculation of the effective interaction parameters in the LDA+U method, *Phys. Rev. B* **71**, 035105 (2005).
- [36]S.W. Cheong and M. Mostovoy, Multiferroics: a magnetic twist for ferroelectricity, *Nat. Mater.* **6**, 13 (2007).
- [37]R. Fei, W. Kang, and L. Yang, Ferroelectricity and Phase Transitions in Monolayer Group-IV Monochalcogenides, *Phys. Rev. Lett.* **117**, 097601 (2016).
- [38]J. Gou, H. Bai, X. Zhang, Y.L. Huang, S. Duan, A. Ariando, S.A. Yang, L. Chen, Y. Lu, and A.T.S. Wee, Two-dimensional ferroelectricity in a single-element bismuth monolayer, *Nature*, (2023).
- [39]D.L. Bao, A. O'Hara, S. Du, and S.T. Pantelides, Tunable, Ferroelectricity-Inducing, Spin-Spiral Magnetic Ordering in Monolayer FeOCl, *Nano Lett.* **22**, 3598 (2022).
- [40]J.-J. Zhang, L. Lin, Y. Zhang, M. Wu, B.I. Yakobson, and S. Dong, Type-II Multiferroic Hf₂VC₂F₂ MXene Monolayer with High Transition Temperature, *J. Am. Chem. Soc.* **140**, 9768 (2018).
- [41]B. Li, Z. Wan, C. Wang, P. Chen, B. Huang, X. Cheng, Q. Qian, J. Li, Z. Zhang, and G. Sun, Van der Waals epitaxial growth of air-stable CrSe₂ nanosheets with thickness-tunable magnetic order, *Nat. Mater.* **20**, 818 (2021).
- [42]B. Huang, G. Clark, E. Navarro-Moratalla, D.R. Klein, R. Cheng, K.L. Seyler, D. Zhong, E. Schmidgall, M.A. McGuire, and D.H. Cobden, Layer-dependent ferromagnetism in a van der Waals crystal down to the monolayer limit, *Nature* **546**, 270 (2017).
- [43]T. Okubo, S. Chung, and H. Kawamura, Multiple-q States and the Skyrmion Lattice of the Triangular-Lattice Heisenberg Antiferromagnet under Magnetic Fields, *Phys. Rev. Lett.* **108**, 017206 (2012).
- [44]P.E. Blöchl, Projector augmented-wave method, *Phys. Rev. B* **50**, 17953 (1994).
- [45]G. Kresse and D. Joubert, From ultrasoft pseudopotentials to the projector augmented-wave method, *Phys. Rev. B* **59**, 1758 (1999).
- [46]G. Kresse and J. Furthmüller, Efficient iterative schemes for ab initio total-energy calculations using a plane-wave basis set, *Phys. Rev. B* **54**, 11169 (1996).
- [47]G. Kresse and J. Furthmüller, Efficiency of ab-initio total energy calculations for metals and semiconductors using a plane-wave basis set, *Comp. Mater. Sci.* **6**, 15 (1996).
- [48]I.V. Solovyev, P.H. Dederichs, and V.I. Anisimov, Corrected atomic limit in the local-density approximation and the electronic structure of d impurities in Rb, *Phys. Rev. B* **50**, 16861 (1994).
- [49]L.M. Sandratskii, Noncollinear magnetism in itinerant-electron systems: theory and applications, *Adv. Phys.* **47**, 91 (1998).
- [50]R.D. Kingsmith and D. Vanderbilt, Theory of Polarization of Crystalline Solids, *Phys. Rev. B* **47**, 1651 (1993).
- [51]G. Henkelman, B.P. Uberuaga, and H. Jónsson, A climbing image nudged elastic band method for finding saddle points and minimum energy paths, *J. Chem. Phys.* **113**, 9901 (2000).
- [52]S. Grimme, Semiempirical GGA-type density functional constructed with a long-range dispersion correction, *J. Comput. Chem.* **27**, 1787 (2006).

- [53]J.P. Perdew, K. Burke, and M. Ernzerhof, Generalized Gradient Approximation Made Simple, Phys. Rev. Lett. **77**, 3865 (1996).
- [54]L. Shulenburger, A.D. Baczewski, Z. Zhu, J. Guan, and D. Tománek, The Nature of the Interlayer Interaction in Bulk and Few-Layer Phosphorus, Nano Lett. **15**, 8170 (2015).